

Geochronology, geochemistry and Sr-Nd, Hf-O isotope systematics of the Linte massif, Adamawa - Yade domain, Cameroon: Implications on the evolution of the Central African Fold Belt

Bovari Syrien Yomeun ^{a,b}, Wei Wang ^{a,*}, Michele Sandra Kamguia Kamani ^{a,b}, Jean Pierre Tchouankoue ^b, Ying-De Jiang ^c, Si-Fang Huang ^a, Kevin Igor Azeuda Ndonfack ^{b,d}, Er-Kun Xue ^a, Gui-Mei Lu ^a, Emmanuel Archelaus Afanga Basua ^{a,b}

^a State Key Laboratory of Geological Processes and Mineral Resources, School of Earth Sciences, China University of Geosciences, Wuhan 430074, China

^b Department of Earth Sciences, University of Yaoundé I, P.O. Box 812, Yaoundé, Cameroon

^c Guangzhou Institute of Geochemistry, Chinese Academy of Sciences, Guangzhou, China

^d School of Civil and Environmental Engineering, University of Science and Technology Beijing, Beijing 100083, China

ARTICLE INFO

ABSTRACT

Keywords:

Linte syenitic massif
Central African Fold Belt
Neoproterozoic plutonism
Pan-African orogeny
Shoshonitic
Subduction-collision setting

The Central African Fold Belt (CAFNB) holds a key position in understanding the process and implications of the Pan-African orogeny in central Africa. However, it has not been fully understood as geological information on some vital domains is not yet available. The Linte massif in the Adamawa-Yade, one of the unrepresented terranes, was investigated and its whole rock geochemical, zircon U-Pb geochronology and Hf-O isotope characteristics and whole rock Sr-Nd data are presented and discussed here. The Linte massif is largely constituted of syenite and subordinate monzonite. The zircon U-Pb dating reveals three major ages at 660, 630 and 600 Ma, indicating a protracted magmatism which lasted at least 60 Ma, during the Neoproterozoic. The rocks are shoshonites, I-type and metaluminous. They have high LILEs (Cs, Rb, Ba and Sr), HFSEs (Th and U) and LREE contents. Their Nb/U, Ta/U, Ce/Pb, Th/La and Th/U ratios, $\delta^{18}\text{O}_{\text{zm}}$ (5.3–7.6‰) and zircon $\epsilon\text{Hf(t)}$ (−14.7 to +3.2), point toward predominantly crustal with or without a mantle component in the sources. The negative $\epsilon\text{Nd(t)}$ values (−8.1 to −10.0), Paleoproterozoic Nd-T_{DM} model ages (ca. 1700–1900 Ma), Hf-T_{DM2} ages of ca. 1300–2400 Ma of zircon grains in Neoproterozoic rocks underline their derivation from Mesoproterozoic to Paleoproterozoic basement rocks.

The lithospheric mantle-generated heat facilitated partial melting in the sources region, as inferred from the shoshonitic affinity and the subduction-related geochemical features (Nb, Ta and Ti depletion). A mainly crustal source with a minor mantle component is inferred for the 660 Ma magmatism and for the 630 Ma rocks emplaced during crustal thickening. On the other hand, the 600 Ma (youngest) magmatic rocks were derived from a crustal source. We infer a subduction-collision setting for the Linte massif during the 660–600 Ma interval. The 630–600 Ma interval of the culmination of collision is consistent with the timing of the main convergence of the Brasiliano Orogeny recorded in South America (~630–600 Ma), suggesting continuation of tectonic features into the western Gondwana.

1. Introduction

The ca. 640 to 540 Ma Pan-African orogeny encompasses a number of Neoproterozoic cratons that amalgamated to form the Gondwana supercontinent (Trompette, 1997; Kröner and Stern, 2004; Neves, 2003; Van Schmus et al., 2008). However, in some areas, the duration of this orogeny is much longer and spans ca. 900–550 Ma (e.g., Caby, 2003;

Valeriano et al., 2004; Berger et al., 2011; Johnson et al., 2011; Pimentel et al., 2011). The Pan-African orogeny in the East Gondwana Block (Africa, South America and eastern Antarctica) is largely manifested in the closure of the Neoproterozoic Oceans such as the Adamastor Ocean (between Africa and South America), the Damara Ocean (between the Kalahari and Congo cratons), the Trans-Sahara Ocean (between the West African craton and the Saharan metacraton) and the Mozambique Ocean

* Corresponding author.

E-mail address: wwz@cug.edu.cn (W. Wang).

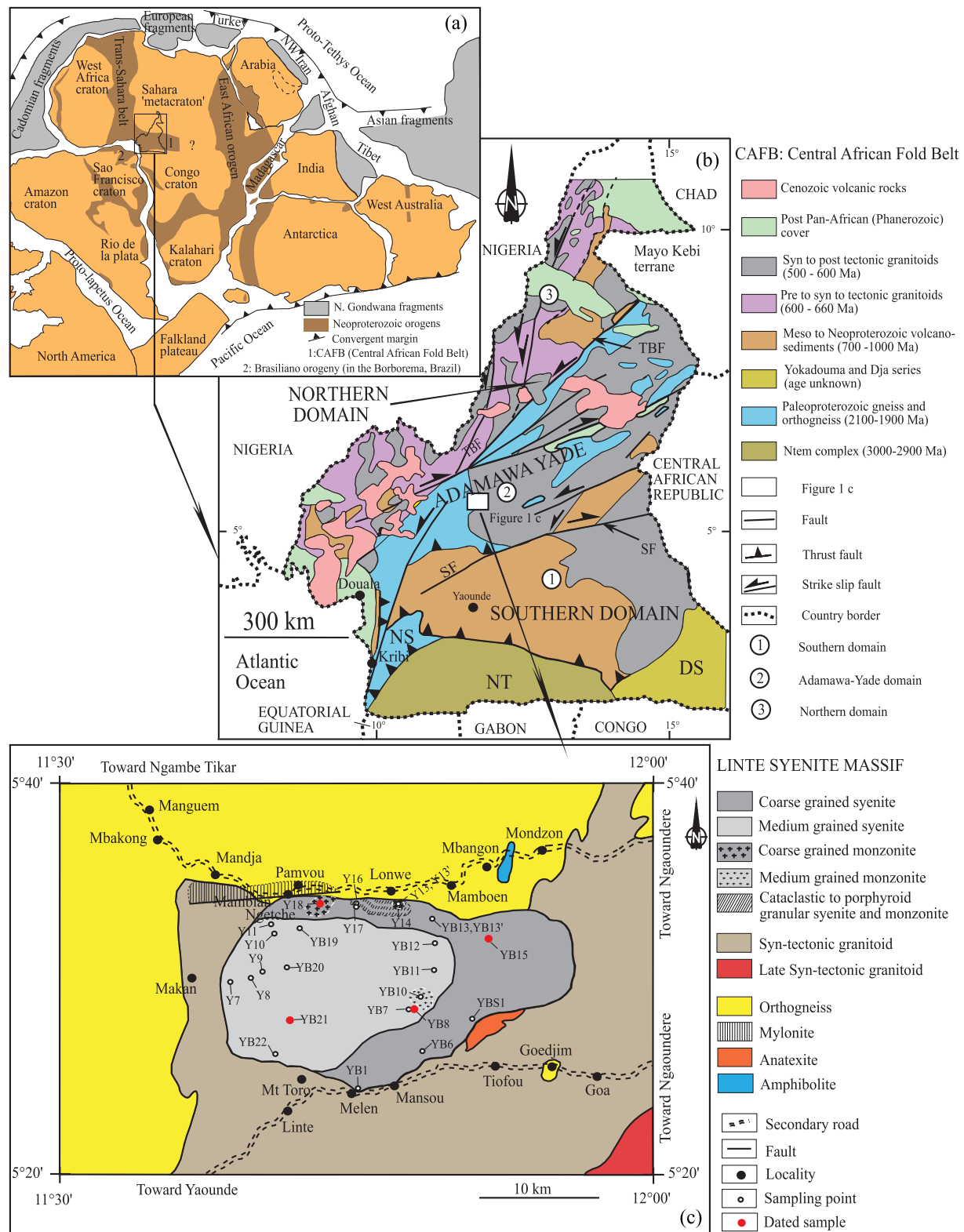


Fig. 1. (a) Schematic reconstitution of Gondwana supercontinent at ca. 540 Ma (adapted after Kusky et al., 2003; Kröner and Stern, 2004; Wang et al., 2019, and references therein). (b) Geological map of Cameroon showing the major lithotectonic domains (compiled from Toteu et al., 2001; Van Schmus et al., 2008; Kwékam et al., 2010, 2013). SF (Sanaga fault), TBF (Tchollire-Banyo fault), NT (Ntem complex), DS (Dja group), NS (Nyong group). (c) Study area, modified from Weecksteen (1957).

(between East Gondwana (Australia, Antarctica, southern India) and West Gondwana (Africa, South America)) (Kröner and Stern, 2004), triggered by collision of eastern and western Gondwana (Fig. 1a). There is a general agreement that the Pan-African orogeny in Central Africa resulted in the convergence of the Congo and West-African cratons with the Saharan metacraton (e.g., Castaing et al., 1994; Trompette, 1997; Abdelsalam et al., 2002; Toteu et al., 2004; Ngako et al., 2008; Liégeois et al., 2013; Kanouo et al., 2021). The collision built up the Pan-African North-Equatorial Fold Belt (Nzenti et al., 1988), also called the Central African Fold Belt (CAFB) (Penaye et al., 2004) which extends from east Nigeria, to Cameroon, south of Chad and Central African Republic, and is bordered to the south, north, west and east by the Archaean Congo craton, the Saharan metacraton, the coeval Trans-Saharan orogenic belt (Abdelsalam et al., 2002; Kröner and Stern, 2004) and the East African belt, respectively (Fig. 1a). The CAFB is postulated to extend into northeast Brazil in the Borborema Province, in the pre Gondwana breakup scenario (Fig. 1a) where it forms part of the Brasiliano Orogeny (Almeida et al., 1981; Toteu et al., 2001; Lerouge et al., 2006; Van Schmus et al., 2008) at ca. 650–550 Ma (Silva Filho et al., 2010). A three-stage evolution of CAFB in Cameroon has been postulated by Ngako et al. (2008) that involve successive collisional and post-collisional tectonic events, namely (1) early crustal thickening producing folds and nappes (ca. 630–620 Ma) due to thrusting and shortening; (2) transcurrent regional shearing with left lateral wrench movement (613–585 Ma) (Ngako et al., 2008) followed by (3) right lateral wrench movements (ca. 585–540 Ma) (Ngako et al., 2008). However, its evolution is debated on account of two alternative models proposed: (1) The “continent–continent collision” model (e.g., Toteu et al., 2004; Penaye et al., 2006; Toteu et al., 2006a, b; Bouyo Houketchang et al., 2009) involving a collision between the northern edge of the Congo craton and its associated Paleoproterozoic series (a passive margin) representing the southern block, and the north-central Cameroon active margin (mobile zone constituted of Adamawa-Yade and west Cameroon domains) representing the northern block. The result of this collision is the delamination of the continental lithospheric mantle, the thrusting of the active margin onto the craton and the presence of huge volume of crustal derived granitoids triggered by the upwelling of asthenosphere (Toteu et al., 2004). (2) The “three-plate collision” model (Ngako et al., 2008; Ngako and Njonfang, 2011) involving the collision between the São Francisco-Congo Craton (SFCC), the eastern Saharan block (ESB), and the West African Craton (WAC). The north–south collision between the ESB and the northern active margin of the SFCC differentiated into a basin and terrane overriding a subduction zone (Ngako et al., 2008), has led to an indent and important crustal deformation in the Cameroon domain and north-western regions. Tectonic events recorded in this active margin have been summarized as the three-stage evolution of CAFB announced above, with the late tectonic right lateral wrench movements resulting from the convergence of the WAC (Ngako and Njonfang, 2011). A lack of relevant data on the CAFB domains in Cameroon makes it difficult to verify these models. The geochemical data of rocks involved in the CAFB indicate a partial or total subduction related origin (e.g., Toteu et al., 2006a; Tchameni et al., 2006; Penaye et al., 2006; Djouka-Fonkwé et al., 2008; Ngo Belnoun et al., 2013; Kwékam et al., 2013, 2019, 2020; Tchouankoué et al., 2016; Gentry et al., 2021; Tchakounté et al., 2021). However the orientation of this subduction is controverted; it could be either a southward subduction (e.g., Ngako and Njonfang, 2011), or a northward subduction (e.g., Toteu et al., 2006a; Gentry et al., 2021; Tchakounté et al., 2021).

Structural and geochronological studies on the CAFB domains in Cameroon (e.g. Njiekak et al., 2008; Tchouankoué et al., 2016; Li et al., 2017; Nomo et al., 2017; Ganwa et al., 2018; Kwékam et al., 2019; Saha-Fouotsa et al., 2019; Kamguia Kamani et al., 2021) have identified the 660–580 Ma period to be the initial to paroxysmal phase of the Pan-African orogeny in the area, resulting in two main components; metamorphic rocks that typify the Yaounde Nappe thrusted onto the Congo Craton in the southern domain, and plutonic rocks characteristic of the

Adamawa-Yade domain and parts of the Cameroon territory, to the west of the Tchollire-Banyo Fault (TBF) (Fig. 1b).

The Linte syenitic massif is located close to the TBF corridor, at the transition between the Adamawa-Yade and northern domains. Till date, the geological information on this massif is limited to the reconnaissance mapping and petrography by Weecksteen (1957) and petrogenetic and tectonic setting studies based on trace element compositions of zircon grains (Ayonta Kenne et al., 2021). Despite its large areal extent (ca. 28 km long) and the fact that syenitic and shoshonitic rocks are scarce in the Pan-African domain of Cameroon, the massif has not received due attention in terms of geochemistry and geochronology. The occurrence of shoshonitic plutonic massifs in the CAFB and possible continuation into the Borborema Province should be considered relevant in understanding the East and Western Gondwana connection. In this study we present zircon U-Pb geochronology and Hf-O isotope data, whole rock geochemistry and Sr-Nd characteristics of the Linte massif to constrain its petrogenesis and tectonic setting and implications of the CAFB and the Pan-African orogeny.

2. Geological setting

The Pan-African plutonism in Cameroon comprises several granitoids and minor gabbroic rocks, subdivided into rejuvenated and juvenile plutons (Nzenti et al., 2001; Njanko et al., 2006; Djouka-Fonkwé et al., 2008; Kwékam et al., 2010, 2013, 2019; Dawai et al., 2013; Ngo Belnoun et al., 2013; Ganwa et al., 2016; Tchouankoué et al., 2016). Rejuvenated plutons include rocks formed and mainly intruded into the Adamawa-Yade domain which show a pre-Pan-African history with Paleoproterozoic to Archean zircon inheritances (e.g., Ganwa et al., 2016). Juvenile granitoids are calc-alkaline, high-K calc-alkaline to shoshonitic and represent plutons with Nd-T_{DM} ages not older than the Paleoproterozoic and typically occur in northern and western Cameroon, to the west of TBF (e.g., Njanko et al., 2006; Djouka-Fonkwé et al., 2008; Kwékam et al., 2010, 2013, 2019; Dawai et al., 2013; Ngo Belnoun et al., 2013; Tchouankoué et al., 2016).

The Pan-African plutonic rocks in Cameroon are bracketed into two main age groups; ca. 660–580 Ma, comprising pre-, syn- to late-tectonic plutons (Toteu et al., 1987, 2001; Kwékam et al., 2010; Dawai et al., 2013) and a younger group (ca. 580–560 Ma) made up of post-tectonic products (e.g., Kwékam et al., 2013; Li et al., 2017). Based on the structural geometry, four major deformation events (D₁ to D₄) have been identified and associated to the 660–560 Ma interval. The earliest D₁ ≥ 620 Ma, D₂ during ca. 620–600 Ma, D₃ at ca. 590–580 Ma and the youngest D₄ at 580–560 Ma (Li et al., 2017). The D₁ event is marked by the flat-lying foliation and could be related to the east-verging early Pan-African nappe tectonics (Toteu et al., 2004). The D₂ event is the result of W-E to WNW-ESE shortening resulting in steep axial plane foliation associated with tight and upright folds and with syn-migmatitic conjugate shear zones (Toteu et al., 2004). The D₃ event could be linked to sinistral movements along the N-S to NE-SW shear zones (Kwékam et al., 2010) while the D₄ is resulted in WSW-ENE to SW-NE dextral shear zones (Toteu et al., 2004; Kwékam et al., 2010).

The Linte massif is located between latitudes 5°20' and 5°40' N and longitudes 11°30' and 12°00' E, at about 260 km N of Yaounde (Fig. 1b). It has an elliptic shape and occupies an area of ca. 360 km² with Neoproterozoic orthogneisses and granitoids cropping out respectively at its northern and southern limits (Fig. 1c). These latters show crystallization ages respectively at 602 Ma and 603 Ma (Yomeun et al., 2022). They crop out as blocks, boulders, domes, and slabs. The orthogneisses show a foliation globally oriented N080 – 090°E and N110 – N120°E, and characterized by discontinuous, blurred, and millimetric alternations of white (quartz-feldspar) and dark (ferromagnesian) layers. They are granoblastic while granitoids are aplites and equigranular to porphyritic. At certain places, granitoids are protomylonites (N135 – 150°E) and characterized by a sub-arrangement of ferromagnesian and ovoid quartz and feldspar crystals. The massif shows a general E-W elongation

Table 1

Codes, locations (GPS), textures, estimated modal compositions (vol. %) and rock types (using the QAP diagram) from the Linte syenitic massif.

Sample code	Sampling site (GPS)	Texture	Estimated modal composition (vol. %)	Rock name (QAP diagram)
YB1	N 05°24'25.8"	Porphyroid granular (coarse grained)	Or: 55, Mc: 10, Pl: 5, Hbl: 15, Bt: 7, Opx: 2, Op: 3, Ttn: 1, Zrn: 1, Ap: 1	Syenite
YBS1	E 011°45'05.1"			
YB6	N 05°24'47.9"		Or: 50, Mc: 15, Pl: 10, Qtz: 5, Hbl: 10, Bt: 5, Opx: 1, Op: 2, Ttn, Zrn and Ap: 2	Syenite
YB13 and YB13'	E 011°46'52.6"		Or: 55, Mc: 10, Pl: 5, Qtz: 3, Hbl: 15, Bt: 5, Opx: 2, Op: 3, Ttn, Zrn and Ap: 2	Syenite
YB15	E 011°48'23.8"		Or: 60, Mc: 5, Pl: 10, Qtz: 1, Hbl: 15, Bt: 5, Op: 2, Ttn, Zrn and Ap: 2	Syenites
Y17	N 05°33'03.2"		Or: 55, Mc: 10, Pl: 10, Qtz: 1 Hbl: 15, Bt: 5, Op: 2, Ttn, Zrn and Ap: 2	Syenite
Y18	E 011°48'52.0"		Or: 55, Mc: 10, Pl: 10, Qtz: 1 Hbl: 15, Bt: 5, Op: 2, Ttn, Zrn and Ap: 2	Syenite
YB7	N 05°28'25.8"	Porphyroid granular (medium grained)	Or: 60, Mc: 5, Pl: 5, Hbl: 20, Bt: 5, Op: 3, Ttn, Zrn and Ap: 2	Syenite
YB8	E 011°43'38.2"			
YB11	N 05°30'26.7"		Or: 60, Mc: 5, Pl: 5, Hbl: 20, Bt: 6, Op: 2, Ttn, Zrn and Ap: 2	Syenite

Table 1 (continued)

Sample code	Sampling site (GPS)	Texture	Estimated modal composition (vol. %)	Rock name (QAP diagram)
YB12	E 011°48'54.2"			
YB19	N 05°31'48.3"		Or: 60, Mc: 5, Pl: 10, Qtz: 1, Hbl: 15, Bt: 5, Op: 2, Ttn, Zrn and Ap: 2	Syenite
YB20	E 011°48'52.4"		Or: 55, Mc: 10, Pl: 10, Qtz: 5, Hbl: 10, Bt: 6, Op: 2, Ttn, Zrn and Ap: 2	Syenite
YB21	N 05°32'38.2"		Or: 60, Mc: 5, Pl: 10, Qtz: 3, Hbl: 12, Bt: 5, Op: 3, Ttn, Zrn and Ap: 2	Syenite
YB22	E 011°42'10.8"		Or: 60, Mc: 5, Pl: 10, Qtz: 1 Hbl: 12, Bt: 5, Op: 3, Ttn, Zrn and Ap: 2	Syenite
Y7	N 05°27'52.7"		Or: 55, Mc: 10, Pl: 10, Qtz: 3, Hbl: 11, Bt: 7, Op: 2, Ttn, Zrn and Ap: 2	Syenite
Y8	E 011°41'00.6"		Or: 55, Mc: 10, Pl: 10, Qtz: 5, Hbl: 10, Bt: 6, Op: 2, Ttn, Zrn and Ap: 2	Syenite
Y9	N 05°30'02.0"		Or: 60, Mc: 5, Pl: 10, Qtz: 3 Hbl: 12, Bt: 5, Op: 3, Ttn, Zrn and Ap: 2	Syenite
Y10	E 011°39'41.3"		Or: 60, Mc: 5, Pl: 10, Qtz: 3 Hbl: 10, Bt: 5, Op: 3, Cpx/ Opx: 2, Ttn, Zrn and Ap: 2	Syenite
Y11	N 05°32'19.5"		Or: 60, Mc: 5, Pl: 10, Qtz: 3 Hbl: 10, Bt: 5, Op: 3, Cpx/ Opx: 2, Ttn, Zrn and Ap: 2	Syenite

(continued on next page)

Table 1 (continued)

Sample code	Sampling site (GPS)	Texture	Estimated modal composition (vol. %)	Rock name (QAP diagram)
			Hbl: 10, Bt: 5, Op: 3, Ttn, Zrn and Ap: 2	
YB10	E 011°40'45.5" N 05°29'04.3"		Or: 35, Mc: 5, Pl: 20, Qtz: 1, Hbl: 22, Bt: 10, Op: 3, Ttn, Zrn and Ap: 4	Monzonite
Y14	E 011°48'16.2" N 05°33'44.5"	Porphyroid granular to subequigranular (protomylonitized coarse grained)	Or: 65, Pl: 5, Hbl: 20, Bt: 5, Op: 3, Ttn, Zrn and Ap: 2	Syenite
Y16	E 011°47'07.5" N 05°33'51.5"		Or: 65, Pl: 5, Qtz: 3, Hbl: 16, Bt: 5, Op: 4, Ttn, Zrn and Ap: 2	Syenite
Y13 and Y13'	E 011°44'59.7" N 05°33'50.9"		Or: 35, Pl: 20, Qtz: 2, Hbl: 20, Bt: 5, Op: 15, Ttn, Zrn and Ap: 3	Monzonites
	E 011°47'07.4"			

(Fig. 1c) which is oblique to the N-S to NE-SW general trend of Pan-African formations in the region.

3. Petrography

According to the modal compositions (Table 1), the dominant type among the rocks of the Linte massif is syenite followed by minor monzonite (Fig. 2). The rocks are mainly undeformed at the macroscopic scale and locally crosscut by joints and quartz-feldspar veins. They crop out as domes and slabs of several tens of meters, boulders and blocks (Fig. 3a, b, c) with sizes varying from centimeter to several tens of meters. Coarse-grained rocks (Fig. 3d) crop out in the southern, northern and eastern parts of the massif (Fig. 1c). Locally, in the northern sector, rocks show incipient deformation and development of protomylonites with granular (Fig. 3e) to subequigranular textures. Medium-grained products (Fig. 3f) are more abundant in the central and western parts of the massif (Fig. 1c).

Syenites are mainly characterized by orthoclase, microcline, plagioclase, quartz, amphibole and biotite with minor clinopyroxene and orthopyroxene. In the central, northern and northwestern parts (Fig. 1c) of the massif, minor monzonites have been observed (Fig. 2). They show ferromagnesian contents slightly higher than syenites and could represent less evolved material of the same series given that on the field and under the naked-eye, these syenites and monzonites are almost similar.

3.1. Syenites

The modal mineralogy of syenites comprises 50–65 vol% orthoclase, 5–15 vol% microcline (when present), 5–10 vol% plagioclase, 1–5 vol% quartz, 10–20 vol% amphibole, 5–7 vol% biotite, 1–2 vol% clino and orthopyroxenes, and 3–8 vol% accessory minerals (opacites, titanite, apatite and zircon) (Table 1). Feldspar, amphibole and biotite grains are anhedral to euhedral micro to megacrysts. Plagioclase, amphibole and biotite are generally wedged between alkali feldspars. Orthoclase crystals have a maximum size of ca. 30 mm. Some of them show oscillatory zoning and are sometimes converted into microclines showing cloudy

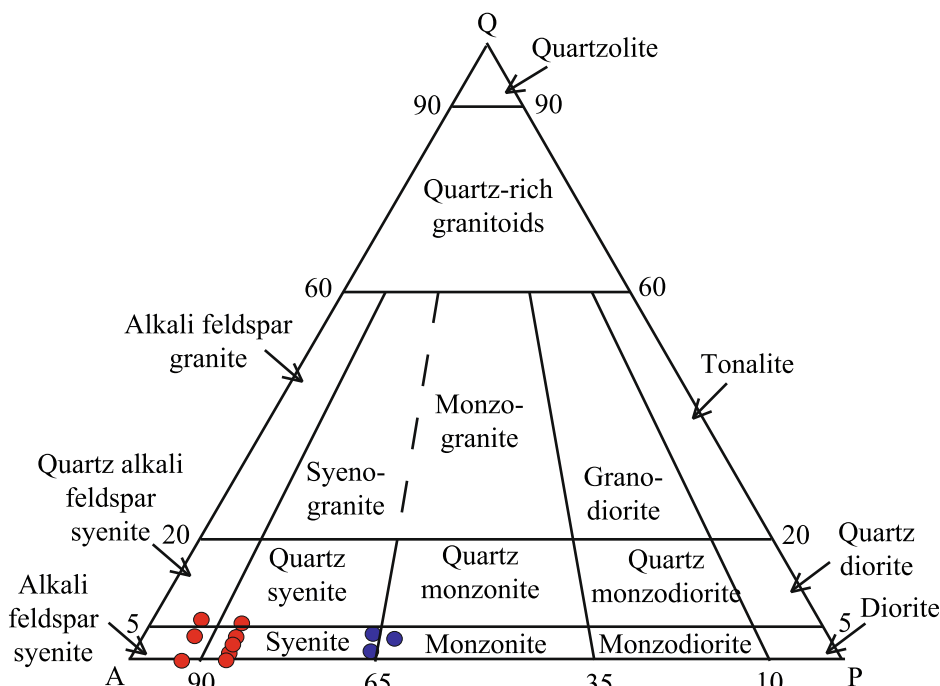


Fig. 2. Petrographical classification (QAP diagram) of the rocks from the Linte massif.

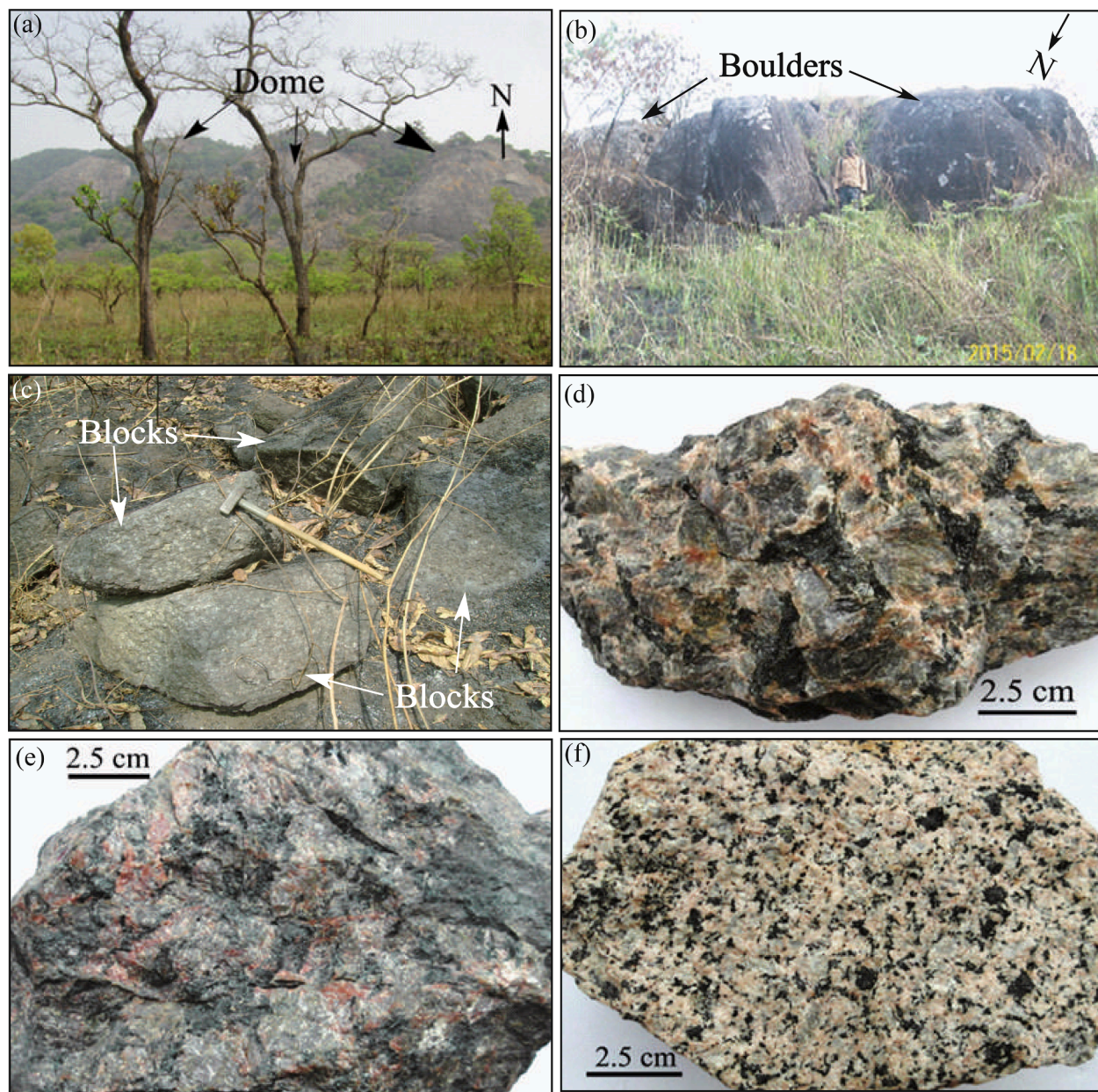


Fig. 3. Selected outcrops and hand samples of rocks from the Linte massif. Outcrops in the shape of: (a) dome, (b) boulder and (c) block (the handle of the hammer is 60 cm along its maximum axis). Hand samples showing porphyroid-granular texture as: (d) coarse -grained, (e) protomylonitized coarse-grained and (f) medium-grained.

cross-hatched twinning due to solid state deformation. In protomylonites, orthoclase appears as cracked, fragmented (Fig. 4a) or slightly deformed crystals. These alkali feldspars show typical perthitic microstructures (Fig. 4b). They also show intragranular microfractures filled with quartz. Plagioclase phenocrysts can reach 2.7 mm. Sometimes they show a cloudy pattern due to intense sericitization (Fig. 4c). They can show chessboard texture (Fig. 4d) and slightly deformed twinning (probably dislocated or disconnected) which is indicative of plastic deformation at high temperature. Myrmecite can occur at K-feldspar-plagioclase contact projecting into K-feldspar. It indicates a possible solid-state deformation and metasomatism. Quartz is interstitial (Fig. 4e), uncommon and mainly represented by crystals not exceeding 1.5 mm. Even in quartz, chessboard microstructure has been observed (Fig. 4f), indicative of deformation at relatively high temperature ($>500^{\circ}\text{C}$). Amphibole is mostly green hornblende. The most developed can locally reach 3.2 mm. Crystals are isolated or clustered in

aggregates. Sometimes they show zonation (Fig. 4g) and partial biotitization as a result of hydrothermal alteration. Biotite flakes (attaining a maximum of 3.15 mm) are isolated and/or associated with other ferromagnesian minerals (Fig. 4h). Larger flakes are locally skeleton-like (Fig. 4h) and display partial chloritization. They can show bent cleavages which are also indicatives of plastic deformation at high temperatures. Clino and orthopyroxene are subhedral to euhedral (Fig. 4e), micro to phenocrysts attaining 1.3 mm. Opaques, titanite, apatite and zircon are mainly interstitial, or included in larger crystals.

3.2. Monzonites

Monzonites approximately display the same petrographic characteristics (size, shape, texture and mineral substitution) as syenites, and they mainly differ in their estimated modal composition (Table 1). They show relatively less orthoclase (30–35 vol%) and microcline (~5 vol%

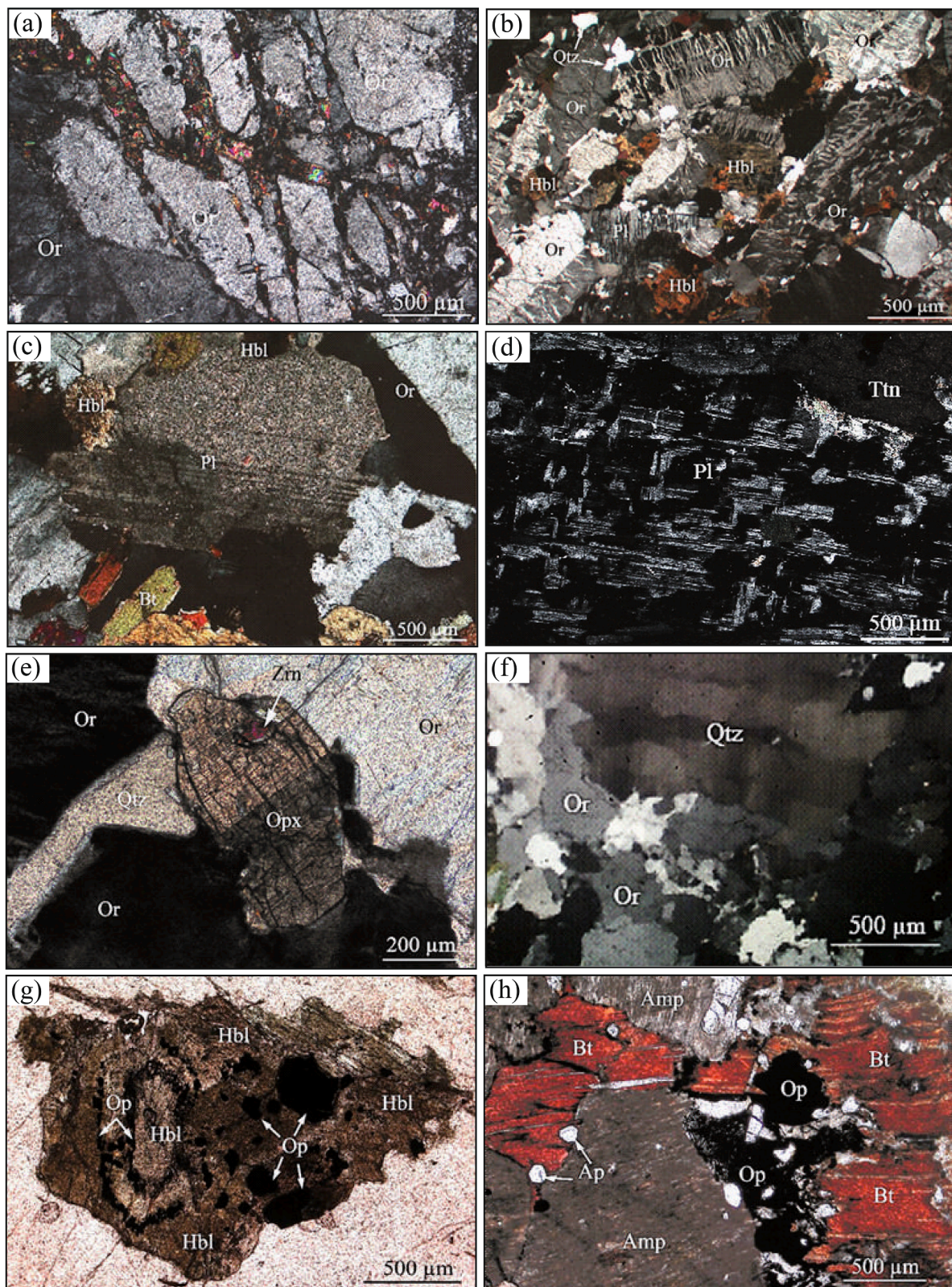


Fig. 4. Microphotographs of syenites (a, b, c, d, e and f under crossed polarized light; g and h under polarized light). (a) Fragmented porphyroclasts of Or showing dense cracks filled with ferromagnesian minerals in protomylonitized syenites. (b) Euhedral and subhedral perthitized Or. (c) Pl in process of sericitization. (d) A portion of Pl phenocryst showing chessboard microstructure. (e) Interstitial Qtz and crystal of Opx jammed between Or crystals (arrow shows Zrn inclusion). (f) Qtz crystal showing chessboard microstructure. (g) Phenocryst of Hbl bearing numerous Op inclusions and showing zonation materialized by the concentric disposition of Op. (h) Skeleton-like Bt showing wide cleavages filled with products of alteration; arrows show semi-inclusions of Ap in Bt and dark Amp. Mineral abbreviations: Or (orthoclase), Mc (microcline), Pl (plagioclase), Qtz (quartz), Amp (amphibole), Hbl (hornblende), Bt (biotite), Ap (apatite), Op (opaque minerals) and Zrn (zircon).

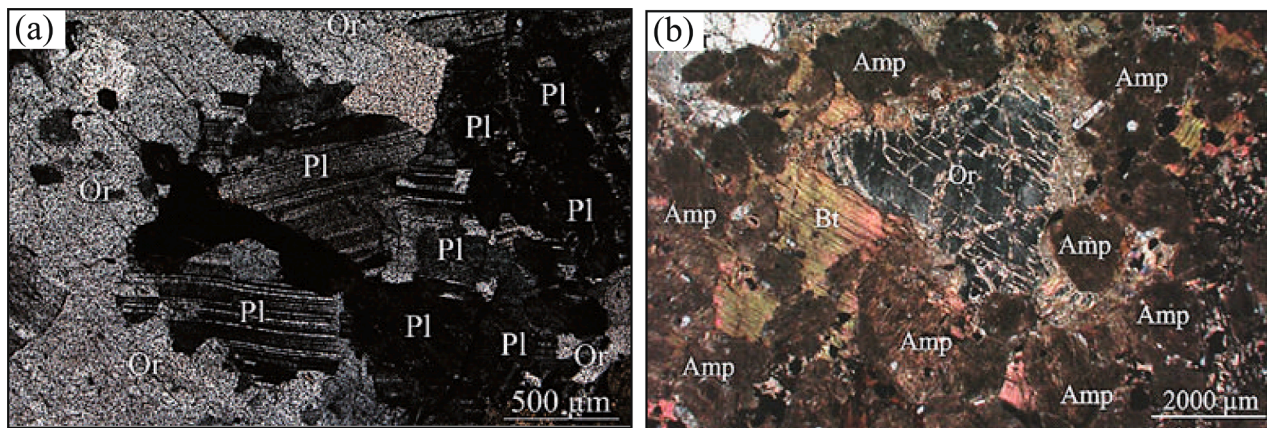


Fig. 5. Microphotographs of monzonitic rocks (a and b under crossed polarized). (a) Anhedral and subhedral crystals of Pl. (b) A cluster of dark Amp merged with Bt flakes around Or. Mineral abbreviations: Or (orthoclase), Pl (plagioclase), Amp (amphibole) and Bt (biotite).

when observed), and more abundant plagioclase (15–20 vol%) (Fig. 5a), amphibole (20–25 vol%) (Fig. 5b), biotite (5–10 vol%) and opaque minerals (3 to 15 vol%). They also contain quartz in small proportions (1–2 vol%) and accessories like titanite, apatite and zircon (3–4 vol%).

4. Analytical methods

Twenty two syenite and four monzonite samples from the Linte massif were analyzed for whole-rock geochemistry. Among them, five syenite and one monzonite samples were selected for whole-rock Sr-Nd isotopic analyses and three syenite (YB21, YB8 and YB15) and one monzonite (Y18) samples were analyzed for zircon U-Pb geochronological and Hf-O isotopic analyses.

Zircon grains were separated by standard crushing, sieving, magnetic and heavy liquid separation methods. Individual grains were hand-picked with the help of binocular microscope and mounted in epoxy resin together with the reference zircons (Penglai and Qinghu), and polished to expose 2/3 of the surface of the crystals. Zircon grains were imaged in reflected and transmitted light to observed internal features. Cathode-Luminescence (CL) images were produced using a Gatan Mono CL4 Cathode-Luminescence detector attached to a Zeiss Sigma 300 field emission SEM at State Key Laboratory of Geological Process and Mineral Resources (SKLGPGR), China University of Geosciences (CUG), Wuhan.

4.1. Zircon oxygen isotopes

Zircon O-isotope analysis was conducted using a Cameca IMS 1280-HR high-precision secondary ion mass spectrometer (SIMS) at the SIMS Laboratory, Guangzhou Institute of Geochemistry, Chinese Academy of Sciences. The Penglai zircon (Li et al., 2010; Yu et al., 2020) was used as an external reference material for calibration and instrumental mass fractionation. The Qinghu zircon (Li et al., 2013) was used as the unknown sample which yielded $\delta^{18}\text{O}$ values of 5.8–6.1‰ (Supplementary material 1) which is in close agreement, within error (2σ) to the recommended value ($5.4\text{\textperthousand} \pm 0.2\text{\textperthousand}$; Li et al., 2013). Details on the analytical method are found in Yang et al. (2018).

4.2. LA-ICP-MS zircon U-Pb ages and Hf isotope analysis

U-Pb isotopic analysis was carried out using LA-ICP-MS at the State Key Laboratory of Geological Processes and Mineral Resources (SKLGPGR), China University of Geosciences (CUG), Wuhan. An Agilent 7500a ICP-MS instrument equipped with a 193 nm ArF excimer laser ablation system was used to acquire ion-signal intensities. Analyses were conducted with a beam diameter of 32 μm , 5 Hz repetition rate for 45 s. Helium was used as the carrier gas. Details on operating conditions for

the instrument and data reduction are provided in Liu et al. (2010). Zircon 91,500 was used as external standard and was analyzed twice every 5 analyses. GJ-1 was analyzed as unknown sample to maintain analytical precision. The obtained $^{206}\text{Pb}/^{238}\text{U}$ ages for this latter reference material are presented in Supplementary material 2. They are consistent with the recommended value of 599.8 ± 1.7 Ma (Jackson et al., 2004). Raw data reduction analyses have been made off-line using ICPMSDataCal (Liu et al., 2010) and the results reported with 1σ error. Concordia diagrams and weighted mean calculations were prepared using Isoplot 4.15 (Ludwig, 2012).

Zircon Lu-Hf isotope analysis were carried out on the grains that were previously analyzed for U-Pb dating (except those showing low concordances), using a Neptune plus multi-collector (MC)-ICPMS system coupled with a Geolas 193 nm ArF excimer laser ablation system at the SKLGPGR (CUG, Wuhan). The prerequisites were laser beam energy density of 5.3 J/cm^2 and a repetition rate of 8 Hz with a spot size of 44 μm diameter and 20 s ablation time. Helium mingled with argon was used as the carrier gas to transport the ablated materials to the MC-ICPMS system. Details on operating conditions can be found in Hu et al. (2012). Zircon reference material, Plešovice and Penglai were used as the unknown samples to ensure the accuracy and precision of analyses. Their measurements yielded $^{177}\text{Hf}/^{176}\text{Hf}$ ratios from 0.282468 to 0.282495 and from 0.282887 to 0.282917 (Supplementary material 3) which are consistent within errors, with the reported values of 0.282482 ± 13 (Sláma et al., 2008) and 0.282906 ± 0.000010 (Li et al., 2010). Raw data were processed off-line.

4.3. Whole-rock major and trace elements geochemistry

Fresh and alteration free pieces of samples were cleansed, dried and crushed to 200 mesh in an agate mill. Major elements were analyzed on fused glass disks, using an X-ray fluorescence spectrophotometer (XRF-1800) at the State Key Laboratory of Geological Process and Mineral Resources, China University of Geosciences, Wuhan. The Loss on Ignition values were determined on 1 g of rock powder by heating it to 1000 °C for 90 min. The international standards GBW07103, GBW07111, GBW07112, GBW07122 and GBW07123 were used as reference materials to ensure the analytical precision. The results show a better than 5% accuracy.

Trace element were determined by ICPMS (inductively coupled plasma mass spectrometry) on an Agilent 7500a ICP-MS, at SKLGPGR, CUG, Wuhan. For this purpose, 50 ± 1 mg of sample powder was digested by $\text{HF} + \text{HNO}_3$ in Teflon bombs. Closed beakers in high-pressure bombs were used to ensure complete digestion. International standard samples AGV-2, BCR-2, BHVO-2, GSP-2 and RGM-2 were used as reference materials during analyses. Pure Rb standard solution was

Table 2

U-Pb (LA-ICP-MS) and O (SIMS) data for zircon from the Linne syenitic massif.

Spot	Th (ppm)	U (ppm)	Ratio Th/U	Ratio ^{207}Pb / ^{206}Pb	$\pm 1\sigma$ (%)	Ratio ^{207}Pb / ^{235}U	$\pm 1\sigma$ (%)	Ratio ^{206}Pb / ^{238}U	$\pm 1\sigma$ (%)	rho	Age (Ma) ^{207}Pb / ^{206}Pb	$\pm 1\sigma$ (Ma)	Age (Ma) ^{207}Pb / ^{235}U	$\pm 1\sigma$ (Ma)	Age (Ma) ^{206}Pb / ^{238}U	$\pm 1\sigma$ (Ma)	Con. (%)	$\delta^{18}\text{O}$	$\pm 2\sigma$
Syenite sample YB21 (N05°27'52.7", E11°41'39.8")																			
YB21-01	93.23	445.35	0.21	0.120	0.2%	5.348	10.7%	0.320	0.3%	0.47	1961	37	1877	17	1791	15	95%	6.5359	0.1423
YB21-02	148.03	118.80	1.25	0.063	0.2%	0.924	2.9%	0.108	0.1%	0.33	694	72	664	15	659	7	99%	6.0337	0.1563
YB21-03	62.08	50.23	1.24	0.065	0.3%	0.973	4.2%	0.108	0.1%	0.29	783	92	690	22	660	8	95%	6.6232	0.1518
YB21-04	325.52	863.93	0.38	0.121	0.2%	5.389	8.8%	0.320	0.3%	0.51	1974	60	1883	14	1791	13	95%	6.4466	0.1774
YB21-05	285.26	678.45	0.42	0.126	0.2%	5.763	8.8%	0.329	0.3%	0.52	2050	27	1941	13	1834	13	94%	6.6710	0.2406
YB21-06	288.80	1057.45	0.27	0.116	0.2%	4.558	7.0%	0.284	0.2%	0.41	1892	29	1742	13	1612	9	92%	6.0970	0.1111
YB21-07	298.20	1023.40	0.29	0.120	0.2%	5.011	8.2%	0.302	0.2%	0.40	1954	30	1821	14	1699	10	93%	6.4471	0.2180
YB21-08	347.03	1210.15	0.29	0.116	0.2%	4.111	8.6%	0.257	0.2%	0.38	1888	38	1657	17	1472	11	88%	6.4272	0.1627
YB21-09	43.62	112.45	0.39	0.130	0.3%	6.053	11.2%	0.337	0.2%	0.39	2098	35	1983	16	1872	12	94%	6.0626	0.2011
YB21-10	161.38	489.49	0.33	0.124	0.2%	5.606	10.8%	0.327	0.4%	0.60	2017	28	1917	17	1821	18	94%	5.9250	0.1425
YB21-11	6.44	12.87	0.50	0.061	0.6%	0.848	7.2%	0.105	0.3%	0.30	643	213	624	39	644	15	96%	6.3189	0.2033
YB21-12	77.28	170.14	0.45	0.063	0.2%	0.950	2.6%	0.110	0.1%	0.43	709	58	678	13	672	7	99%	6.0596	0.2303
YB21-13	328.64	946.31	0.35	0.112	0.2%	3.861	9.8%	0.247	0.4%	0.60	1828	31	1606	21	1425	20	88%	6.6281	0.2491
YB21-14	290.06	944.14	0.31	0.114	0.2%	4.557	7.7%	0.290	0.2%	0.38	1858	30	1742	14	1639	9	93%	6.4486	0.2596
YB21-15	332.63	960.47	0.35	0.117	0.2%	5.028	9.8%	0.311	0.3%	0.41	1906	37	1824	17	1747	12	95%	5.6572	0.1589
Monzonitic sample Y18 (N05°34'2.3", E11°43'38.2")																			
Y18-01	89.34	94.64	0.94	0.060	0.2%	0.858	2.9%	0.104	0.1%	0.32	617	81	629	16	635	7	99%	6.9254	0.1422
Y18-02	171.83	201.58	0.85	0.062	0.2%	0.875	2.4%	0.103	0.1%	0.29	657	61	638	13	633	5	99%	6.5459	0.1758
Y18-03	90.09	138.32	0.65	0.066	0.2%	1.211	3.4%	0.132	0.1%	0.31	820	56	805	16	800	7	99%	8.1562	0.1844
Y18-04	50.50	27.49	1.84	0.073	1.1%	0.871	11.2%	0.104	0.8%	0.59	1013	300	636	61	637	46	99%	7.2261	0.2148
Y18-05	378.62	449.19	0.84	0.059	0.1%	0.845	1.9%	0.103	0.1%	0.35	569	50	622	11	635	5	97%	7.2376	0.2589
Y18-06	12.03	79.93	0.15	0.060	0.3%	0.823	3.3%	0.101	0.1%	0.30	591	93	610	19	620	7	98%	7.5448	0.1196
Y18-07	139.89	169.37	0.83	0.122	0.2%	5.975	11.6%	0.354	0.3%	0.49	1983	31	1972	17	1955	16	99%	7.7133	0.1988
Y18-08	369.93	541.92	0.68	0.057	0.1%	0.817	2.1%	0.103	0.1%	0.29	502	58	606	11	632	4	95%	7.6260	0.1764
Y18-09	32.30	48.66	0.66	0.060	0.3%	0.852	3.8%	0.104	0.1%	0.27	609	100	626	21	635	7	98%	7.4101	0.2529
Y18-10	167.22	234.24	0.71	0.058	0.1%	0.823	2.1%	0.103	0.1%	0.36	524	49	610	12	633	5	96%	6.8580	0.2040
Y18-11	193.59	261.55	0.74	0.060	0.2%	0.857	3.6%	0.103	0.2%	0.53	617	47	629	20	633	13	99%	6.3833	0.1439
Y18-12	257.24	364.56	0.71	0.059	0.1%	0.840	1.8%	0.103	0.1%	0.37	561	42	619	10	634	5	97%	6.0791	0.2296
Y18-13	151.45	151.74	1.00	0.059	0.2%	0.834	2.3%	0.103	0.1%	0.35	550	61	616	13	634	6	97%	6.7154	0.3156
Y18-14	100.09	93.33	1.07	0.060	0.4%	0.857	5.4%	0.104	0.1%	0.18	611	137	628	30	636	7	98%	6.7379	0.2159
Y18-15	96.08	123.12	0.78	0.061	0.2%	0.881	3.3%	0.104	0.1%	0.31	654	90	642	18	639	7	99%	5.2841	0.1564
Syenite sample YB8 (N05°28'29.8", E11°47'54.6")																			
YB8-01	124.64	99.32	1.25	0.062	0.2%	0.837	3.2%	0.098	0.1%	0.27	676	80	618	18	603	6	97%	7.4839	0.2427
YB8-02	61.31	68.87	0.89	0.061	0.2%	0.807	3.0%	0.097	0.1%	0.34	632	86	601	17	597	7	99%	7.6390	0.1629
YB8-03	145.36	127.36	1.14	0.058	0.2%	0.786	2.5%	0.098	0.1%	0.29	539	64	589	14	602	5	97%	7.3453	0.2271
YB8-04	143.62	109.25	1.31	0.056	0.2%	0.750	2.5%	0.098	0.1%	0.27	454	76	568	15	600	5	94%	7.2460	0.2113
YB8-05	187.10	193.76	0.97	0.067	0.2%	0.910	2.3%	0.099	0.1%	0.35	837	58	657	12	606	5	91%	7.0067	0.1674
YB8-06	286.33	247.25	1.16	0.061	0.3%	0.820	3.2%	0.098	0.1%	0.24	633	55	608	18	604	5	99%	7.2879	0.1852
YB8-07	135.96	126.00	1.08	0.066	0.3%	0.902	4.7%	0.099	0.1%	0.23	817	97	653	25	606	7	92%	7.3288	0.2281
YB8-08	74.24	84.58	0.88	0.060	0.3%	0.811	3.3%	0.098	0.1%	0.28	611	95	603	19	603	7	99%	7.3164	0.1769
YB8-09	81.54	83.80	0.97	0.061	0.3%	0.815	3.3%	0.098	0.1%	0.32	633	95	605	18	605	8	99%	6.9528	0.1257
YB8-10	123.39	112.59	1.10	0.060	0.3%	0.810	3.5%	0.098	0.1%	0.26	611	94	602	19	602	6	99%	7.2655	0.1899
YB8-11	507.24	493.94	1.03	0.076	0.2%	1.030	2.0%	0.098	0.1%	0.47	1096	45	719	10	603	5	82%	7.1727	0.1368
YB8-12	102.23	123.64	0.83	0.063	0.2%	0.855	2.8%	0.098	0.1%	0.33	720	76	627	15	604	6	96%	7.1982	0.1975
YB8-13	203.83	166.47	1.22	0.065	0.2%	0.875	2.4%	0.098	0.1%	0.37	765	66	639	13	605	6	94%	7.1623	0.2048
YB8-14	186.89	141.98	1.32	0.061	0.2%	0.822	2.6%	0.099	0.1%	0.34	620	75	609	15	607	6	99%	6.8501	0.1274

(continued on next page)

Table 2 (continued)

Spot	Th (ppm)	U (ppm)	Ratio Th/U	Ratio ^{207}Pb / ^{206}Pb	$\pm 1\sigma$ (%)	Ratio ^{207}Pb / ^{238}U	$\pm 1\sigma$ (%)	Ratio ^{206}Pb / ^{238}U	$\pm 1\sigma$ (%)	rho	Age (Ma) ^{207}Pb / ^{235}U	$\pm 1\sigma$ (Ma)	Age (Ma) ^{206}Pb / ^{238}U	$\pm 1\sigma$ (Ma)	Con. (%)	$\delta^{18}\text{O}$	$\pm 2\sigma$		
YB8-15	80.56	79.88	1.01	0.063	0.3%	0.857	3.3%	0.099	0.1%	0.33	722	83	629	18	607	7	96%	6.9079	0.2657
Syenite sample YB15 (N05°32'04.7", E11°51'44.2")																			
YB15-01	153.23	144.19	1.06	0.067	0.3%	0.906	3.8%	0.098	0.1%	0.23	835	85	655	20	602	6	91%	6.6399	0.1064
YB15-02	282.05	227.30	1.24	0.060	0.2%	0.809	2.4%	0.098	0.1%	0.30	594	69	602	14	603	5	99%	6.5590	0.1605
YB15-03	214.30	208.05	1.03	0.060	0.2%	0.809	2.0%	0.097	0.1%	0.38	609	54	602	11	598	5	99%	6.7393	0.1915
YB15-04	156.87	159.24	0.99	0.060	0.2%	0.811	2.3%	0.097	0.1%	0.31	613	61	603	13	599	5	99%	6.6448	0.1256
YB15-05	418.29	318.05	1.32	0.061	0.2%	0.821	2.2%	0.098	0.1%	0.37	632	57	609	12	602	6	98%	6.7813	0.1502
YB15-06	228.07	237.84	0.96	0.061	0.2%	0.813	2.0%	0.096	0.1%	0.40	650	51	604	11	591	5	97%	6.6453	0.2254
YB15-07	268.23	186.81	1.44	0.062	0.2%	0.834	2.3%	0.098	0.1%	0.33	661	56	616	13	600	5	97%	6.6709	0.2791
YB15-08	175.77	191.03	0.92	0.059	0.2%	0.788	2.2%	0.098	0.1%	0.34	546	61	590	12	600	5	98%	6.2738	0.1747
YB15-09	158.85	169.04	0.94	0.060	0.2%	0.813	2.2%	0.098	0.1%	0.38	598	57	604	12	604	6	99%	6.6107	0.1556
YB15-10	188.52	189.33	1.00	0.060	0.2%	0.814	2.6%	0.097	0.1%	0.30	617	65	605	14	599	5	99%	6.6025	0.2462
YB15-11	314.22	217.92	1.44	0.059	0.2%	0.791	2.2%	0.098	0.1%	0.33	554	58	592	12	602	5	98%	6.9610	0.1584
YB15-12	200.44	204.02	0.98	0.060	0.2%	0.811	2.2%	0.099	0.1%	0.34	591	62	603	12	605	5	99%	6.3488	0.1107
YB15-13	226.71	239.81	0.95	0.057	0.1%	0.774	2.0%	0.098	0.1%	0.34	509	56	582	11	600	5	96%	6.3522	0.1721
YB15-14	211.16	197.90	1.07	0.062	0.2%	0.839	2.1%	0.098	0.1%	0.37	687	56	618	12	601	5	97%	6.4767	0.1947
YB15-15	211.11	222.16	0.95	0.058	0.2%	0.773	2.1%	0.098	0.1%	0.33	509	59	582	12	600	5	96%	6.2400	0.1648

used for internal calibration. Analytical precision for ICP-MS analyses are better than 5% for most trace elements.

4.4. Whole-rock Sr-Nd isotopic analyses

Whole-rock Sr-Nd isotopic analysis were performed through a Finnigan Triton Ti thermal ionization mass spectrometer (TIMS) at SKLGPMPR, CUG, Wuhan. About 100 mg powder of samples was dissolved in a mixture of concentrated HF + HNO₃ in a Teflon capsule. After desiccation at 190 °C in an oven for 48 h, the residue was treated with 1 ml of 6 N HCl and dissolved in 1 ml of 2.5 N HCl. Elemental Nd was isolated and purified from the final solution through the conventional cation-exchange technique. The mass fractionation correction for measured Nd isotopic ratios was based on ¹⁴⁶Nd/¹⁴⁴Nd value of 0.7219. USGS reference material BCR-2 yielded ¹⁴³Nd/¹⁴⁴Nd ratio of 0.512655 ± 4. The λ (decay constant) value of 6.54×10^{-12} year for ¹⁴⁷Sm was considered for the calculation (Lugmair and Marti, 1978). The εNd(t) values have been calculated taking into account the chondritic uniform reservoir for a present-day ¹⁴³Nd/¹⁴⁴Nd ratio of 0.51263 and ¹⁴⁷Sm/¹⁴⁴Nd ratio of 0.196 (Bouvier et al., 2008). Nd-T_{DM} model age calculations were referred to ¹⁴³Nd/¹⁴⁴Nd and ¹⁴⁷Sm/¹⁴⁴Nd ratios of 0.513151 and 0.2136 (Liew and Hofmann, 1988) respectively, for the present-day depleted mantle.

5. Results

5.1. U-Pb zircon geochronology

The U-Pb isotope data on the four analyzed samples (syenite: YB21, YB8 and YB15 and monzonite Y18) are presented in Table 2.

Zircon grains from syenite sample YB21 (Fig. 1c) are subhedral to euhedral, and 150 to 300 µm in length, and often have resorbed margins. They are dark, zoned (oscillatory zoning) and under CL sometimes display bright rims of variable thickness (Fig. 6a). Their high Th/U ratios (0.2 to 1.2) and presence of oscillatory zoning indicate magmatic origin (e.g., Rubatto and Gebauer, 2000; Belousova et al., 2002; Corfu et al., 2003; Wu and Zheng, 2004). Grains with recrystallization rims have a lower uranium concentration (U = 13–170 ppm). Fifteen spots analyzed on 13 zircon grains define a Concordia line with lower and upper intercepts at 667 ± 75 Ma and 2064 ± 41 Ma (MSWD = 2.3; Fig. 6a). A small group of four zircon grains plots on the lower intercept and are consistent with a ²⁰⁶Pb/²³⁸U concordant age of 662 ± 4 Ma (MSWD = 1.1; Fig. 6a), which is similar (within error) to the 667 ± 75 Ma. Thus, 2064 ± 41 Ma and 662 ± 4 Ma could be interpreted as the protolith age and the age of the magmatic event materialized by a crystallization, respectively.

Zircon grains from the monzonite sample Y18 (Fig. 1c) are mostly euhedral and prismatic, 200–450 µm in length and display dark to light luminescence, and clear or cloudy oscillatory zoning under CL (Fig. 6b). Some of them show bright recrystallization rims of variable thickness. Their Th/U ratios range from 0.7 to 1.8, indicating a magmatic origin. Fifteen analyses, conducted on fourteen zircon grains yielded thirteen ²⁰⁶Pb/²³⁸U ages between 620 and 639 Ma (Fig. 6b). Among these, twelve yielded a concordant age of 633 ± 2 Ma (MSWD = 11.7; Fig. 6b) with a consistent weighted mean age of 633 ± 3 Ma (MSWD = 0.4 Fig. 6b) which we interpret as the crystallization age. Two analyses yielded older ages (800 Ma and 1983 Ma) that likely represent xenocrystic grains inherited from the source and/or country rocks.

Zircon grains from the syenite sample YB8 (Fig. 1c) are broken and anhedral with length varying between 200 and 350 µm. Most of them show light luminescence while some display banded zoning under CL (Fig. 6c). Their high Th/U ratios (0.8 to 1.3) indicate a magmatic origin. Fifteen spots on fifteen grains were performed amongst which fourteen yielded concordant (concordance degree 91–99%) ²⁰⁶Pb/²³⁸U ages between 597 and 607 Ma, concordant age of 604 ± 4 Ma (MSWD = 7.9; Fig. 6c) and a weighted mean age of 603 ± 3 Ma (MSWD = 0.2; Fig. 6c),

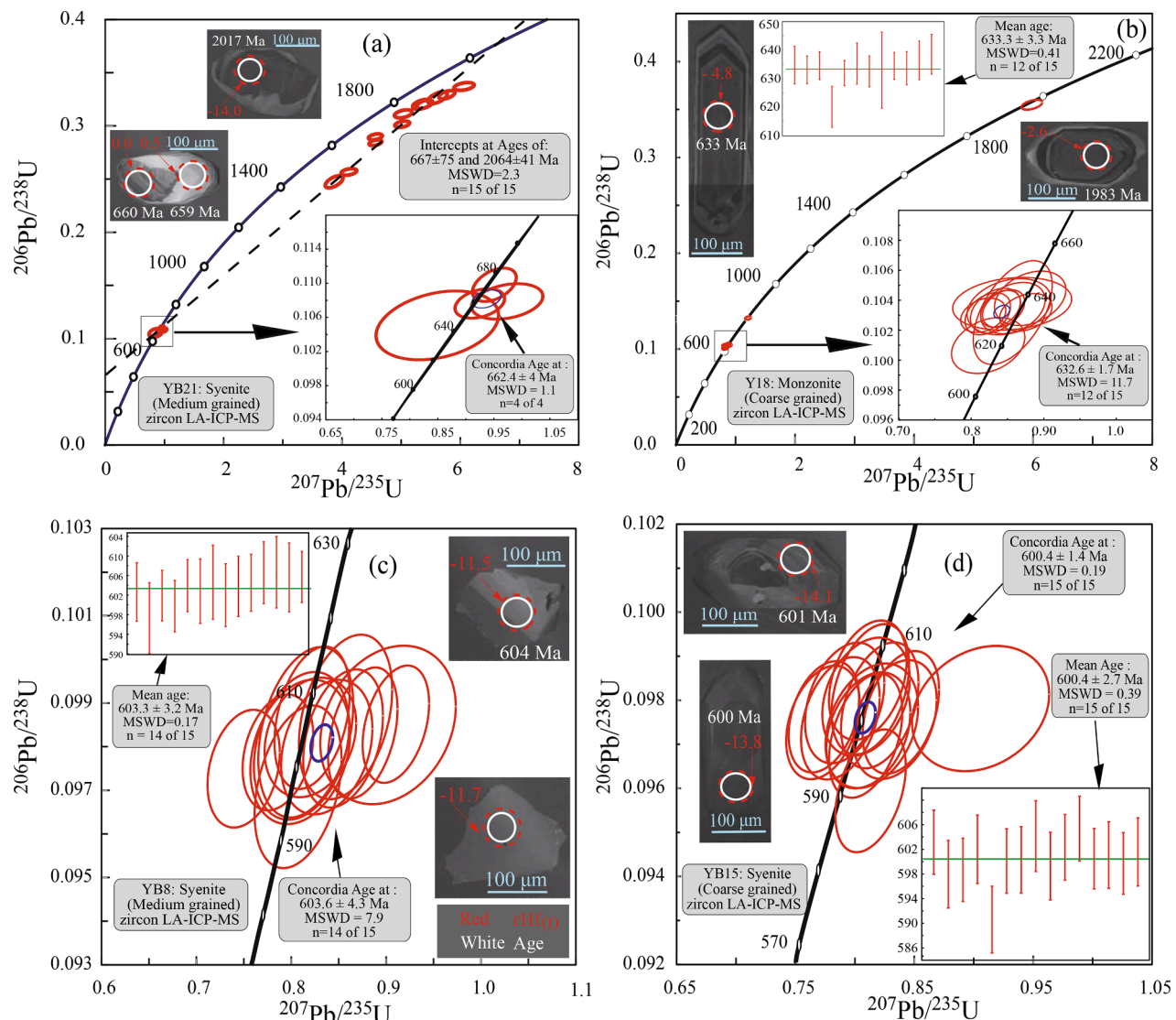


Fig. 6. LA-ICP-MS U-Pb zircon age Concordia diagrams and representative cathode-luminescence (CL) images of dated zircons. (a) syenite sample YB21. (b) monzonite sample Y18. (c) syenite sample YB8. (d) syenite sample YB15. White circles and numbers indicate the spot locations of U-Pb analyses and corresponding ages. Red dashed circles and numbers show the spot locations of Hf isotope analyses and corresponding $\epsilon\text{Hf}(t)$ values. (For interpretation of the references to colour in this figure legend, the reader is referred to the web version of this article.)

that we interpreted as the age of crystallization.

Fifteen selected zircon grains from syenite sample YB15 (Fig. 1c) are mostly euhedral and prismatic, and 200 to 400 μm long. They are slightly dark and show oscillatory zoning under CL (Fig. 6d) which, along with a high Th/U ratio (0.9–1.4) testifies their magmatic origin. They show a good concordance (91–99%) and $^{206}\text{Pb}/^{238}\text{U}$ ages from 591 to 605 Ma, yielding a concordant age of 600 ± 1 Ma (MSWD = 0.2; Fig. 6d), and a weighted mean age of 600 ± 3 Ma (MSWD 0.4; Fig. 6d), which is interpreted as the age of crystallization.

In summary, the four U-Pb zircon ages on the syenite massif suggest crystallization at ca. 660 Ma, 630 Ma and 600 Ma.

5.2. Zircon Hf isotope compositions

In situ Hf isotopic compositions of zircon grains with high concordances (90–100%) from all four dated samples are provided in Table 3. The measured $^{176}\text{Yb}/^{177}\text{Hf}$ ratios of Neoproterozoic zircon grains vary from 0.282376 to 0.282453, 0.282069 to 0.282500, 0.282070 to 0.282107, and 0.282001 to 0.282102, respectively, for zircon grains in samples YB21, Y18, YB8 and YB15. They show relatively low (<0.08

$\text{Yb}^{176}/\text{Hf}^{177}$ ratios and $\epsilon\text{Hf}(t)$ values from +0.0 to +3.0 (YB21), −11.5 to +3.2 (Y18), −12.0 to −10.9 (YB8) and −14.7 to −11.0 (YB15), and corresponding T_{DM2} ages at 1379–1569 Ma, 1345–2084 Ma, 2209–2275 Ma and 2209–2441 Ma, respectively (Table 3). The measured $^{176}\text{Yb}/^{177}\text{Hf}$ ratios of inherited zircon grains vary from 0.281143 to 0.281223 and 0.281487 to 0.282496 in samples YB21 and Y18. The latter ones also show relatively low $^{176}\text{Yb}/^{177}\text{Hf}$ ratios (≤ 0.08) and $\epsilon\text{Hf}(t)$ values from −16.6 to −10.9 (YB21) and −2.6 to 6.6 (Y18) with 3358–3548 Ma and 1260–2766 Ma T_{DM2} ages at, respectively.

5.3. Zircon oxygen isotopes

The zircon oxygen isotope data are shown in Table 2. The $\delta^{18}\text{O}$ values range from 5.3‰ to 7.6‰, with a mean of $6.8 \pm 0.2\%$ ($2\sigma, n = 47$) for Neoproterozoic zircons grains. In the inherited zircons grains, these values vary from 5.7‰ to 8.2‰, with a mean of $6.1 \pm 0.2\%$ ($2\sigma, n = 13$). The $\delta^{18}\text{O}_{\text{Zrn}}$ values are within the range for $\delta^{18}\text{O}$ of typical igneous zircon grains of the continental crust, with a single mantle one value ($5.3 \pm 0.2\%$) (e.g., Valley et al., 2005). Average whole rock $\delta^{18}\text{O}$ ($\delta^{18}\text{O}_{\text{WR}}$) values (Table 4) were calculated (excluding data from inherited zircon

Table 3

Lu-Hf isotopic data of rocks from the Linte syenitic massif.

Spot	Age (Ma)	$^{176}\text{Yb}/^{177}\text{Hf}$	$\pm 2\sigma$	$^{176}\text{Lu}/^{177}\text{Hf}$	$\pm 2\sigma$	$^{176}\text{Hf}/^{177}\text{Hf}$	$\pm 2\sigma$	$^{176}\text{Hf}/^{177}\text{Hf}_{\text{fi}}$	$\epsilon\text{Hf(t)}$	T_{DM1} (Ma)	T_{DM2} (Ma)
Syenite sample YB21 (N05°27'52.7", E11°41'39.8")											
YB21-02	662	0.0249	6.5E-05	0.000651	1.7E-06	0.282376	1.5E-05	0.282368	0.01	1227	1569
YB21-03	662	0.0346	4.8E-04	0.000904	1.3E-05	0.282391	1.5E-05	0.282380	0.46	1213	1541
YB21-11	662	0.00112	1.8E-05	0.000024	5.5E-07	0.282453	1.1E-05	0.282453	3.03	1101	1379
YB21-12	662	0.0292	4.2E-04	0.000735	1.2E-05	0.282438	1.4E-05	0.282429	2.19	1142	1432
YB21-01	1961	0.0570	3.4E-03	0.001336	7.7E-05	0.281223	1.5E-05	0.281173	-12.74	2852	3366
YB21-04	1974	0.0800	3.6E-04	0.001927	1.3E-05	0.281170	1.1E-05	0.281098	-15.13	2971	3521
YB21-05	2050	0.0601	3.9E-04	0.001424	6.2E-06	0.281153	1.3E-05	0.281097	-13.39	2955	3474
YB21-06	1892	0.0510	5.6E-04	0.001208	1.5E-05	0.281153	1.2E-05	0.281110	-16.61	2938	3548
YB21-07	1954	0.0642	2.6E-04	0.001539	7.0E-06	0.281166	1.5E-05	0.281109	-15.18	2945	3509
YB21-09	2098	0.0238	1.5E-04	0.000563	2.1E-06	0.281159	1.2E-05	0.281137	-10.87	2881	3358
YB21-10	2017	0.0448	1.9E-03	0.001073	4.5E-05	0.281143	1.2E-05	0.281102	-14.00	2941	3485
YB21-14	1858	0.0675	5.4E-04	0.001620	1.1E-05	0.281190	1.4E-05	0.281133	-16.55	2918	3518
YB21-15	1906	0.0804	3.6E-04	0.001872	1.0E-05	0.281194	1.5E-05	0.281127	-15.68	2933	3502
Monzonitic sample Y18 (N05°34'2.3", E11°43'38.2")											
Y18-01	633	0.0494	1.4E-03	0.001333	3.9E-05	0.282342	1.2E-05	0.282326	-2.11	1297	1680
Y18-13	633	0.0773	1.2E-03	0.002120	3.5E-05	0.282354	1.3E-05	0.282329	-2.00	1306	1672
Y18-14	633	0.0152	1.1E-04	0.000406	2.9E-06	0.282437	1.4E-05	0.282433	1.67	1133	1442
Y18-15	633	0.0664	1.0E-03	0.001844	2.4E-05	0.282459	1.6E-05	0.282437	1.82	1147	1432
Y18-02	633	0.0774	2.3E-03	0.002003	5.9E-05	0.282500	1.2E-05	0.282476	3.21	1093	1345
Y18-04	633	0.0169	2.2E-04	0.000437	5.9E-06	0.282466	1.3E-05	0.282461	2.66	1095	1379
Y18-05	633	0.0761	2.2E-03	0.002071	6.3E-05	0.282460	1.2E-05	0.282436	1.77	1152	1435
Y18-06	633	0.0169	4.8E-04	0.000483	1.4E-05	0.282393	1.1E-05	0.282387	0.06	1197	1543
Y18-08	633	0.0615	3.6E-03	0.001783	1.1E-04	0.282165	2.7E-05	0.282144	-8.57	1564	2084
Y18-09	633	0.0568	1.4E-03	0.001557	4.2E-05	0.282337	1.4E-05	0.282319	-2.36	1311	1695
Y18-10	633	0.0237	1.0E-03	0.000728	2.9E-05	0.282069	1.3E-05	0.282061	-11.51	1653	2268
Y18-11	633	0.0288	9.2E-04	0.000843	2.8E-05	0.282260	1.4E-05	0.282250	-4.78	1393	1847
Y18-12	633	0.0280	9.3E-04	0.000734	2.1E-05	0.282375	1.2E-05	0.282366	-0.68	1230	1590
Y18-03	800	0.0705	4.2E-04	0.001965	8.6E-06	0.282496	1.5E-05	0.282467	6.64	1097	1260
Y18-07	1983	0.0421	1.0E-03	0.001159	3.0E-05	0.281487	1.3E-05	0.281444	-2.63	2477	2766
Syenite sample YB8 (N05°28'29.8", E11°47'54.6")											
YB8-01	603	0.0182	1.4E-04	0.000458	1.8E-06	0.282075	1.4E-05	0.282070	-11.85	1633	2266
YB8-13	603	0.0388	1.9E-04	0.000964	8.3E-07	0.282107	1.3E-05	0.282096	-10.93	1611	2209
YB8-14	603	0.0412	1.7E-04	0.001021	1.1E-06	0.282087	1.4E-05	0.282075	-11.66	1641	2254
YB8-15	603	0.0227	9.9E-05	0.000583	3.5E-06	0.282079	1.3E-05	0.282073	-11.75	1633	2260
YB8-02	603	0.0120	5.0E-05	0.000310	4.7E-07	0.282070	1.4E-05	0.282066	-11.98	1634	2274
YB8-03	603	0.0234	9.1E-05	0.000579	6.1E-07	0.282078	1.5E-05	0.282072	-11.79	1634	2263
YB8-04	603	0.0238	6.7E-05	0.000595	9.8E-07	0.282075	1.3E-05	0.282068	-11.92	1640	2271
YB8-06	603	0.0361	1.8E-04	0.000890	8.4E-07	0.282085	1.3E-05	0.282075	-11.66	1638	2255
YB8-08	603	0.0167	1.3E-04	0.000435	4.3E-06	0.282077	1.3E-05	0.282072	-11.79	1630	2262
YB8-09	603	0.0216	1.5E-04	0.000557	2.1E-06	0.282084	1.3E-05	0.282078	-11.58	1626	2250
YB8-10	603	0.0305	1.3E-04	0.000768	5.7E-07	0.282081	1.3E-05	0.282072	-11.78	1639	2262
YB8-12	603	0.0171	8.2E-05	0.000441	6.2E-07	0.282086	1.2E-05	0.282081	-11.47	1618	2243
Syenite sample YB15 (N05°32'04.7", E11°51'44.2")											
YB15-02	600	0.0137	4.2E-05	0.000372	1.4E-06	0.282033	1.5E-05	0.282029	-13.37	1687	2359
YB15-11	600	0.0299	4.3E-04	0.000785	9.1E-06	0.282001	1.3E-05	0.281992	-14.68	1750	2441
YB15-12	600	0.0262	2.5E-04	0.000690	6.6E-06	0.282016	1.3E-05	0.282008	-14.10	1724	2404
YB15-13	600	0.0247	2.1E-04	0.000659	5.7E-06	0.282017	1.2E-05	0.282009	-14.06	1722	2402
YB15-14	600	0.0305	2.2E-04	0.000816	8.3E-06	0.282018	1.3E-05	0.282009	-14.07	1727	2402
YB15-15	600	0.0246	1.7E-04	0.000646	4.8E-06	0.282024	1.3E-05	0.282017	-13.80	1712	2386
YB15-03	600	0.0131	2.0E-04	0.000353	3.9E-06	0.282011	1.3E-05	0.282007	-14.14	1716	2407
YB15-04	600	0.0138	8.3E-05	0.000374	1.7E-06	0.282020	1.3E-05	0.282015	-13.85	1706	2389
YB15-05	600	0.0161	1.2E-04	0.000425	2.4E-06	0.282102	1.3E-05	0.282097	-10.97	1596	2209
YB15-06	600	0.0150	1.5E-04	0.000404	3.3E-06	0.282009	1.2E-05	0.282005	-14.23	1721	2413
YB15-07	600	0.0291	6.3E-04	0.000787	1.9E-05	0.282042	1.5E-05	0.282033	-13.23	1693	2350
Spot	Age (Ma)	$^{176}\text{Yb}/^{177}\text{Hf}$	$\pm 2\sigma$	$^{176}\text{Lu}/^{177}\text{Hf}$	$\pm 2\sigma$	$^{176}\text{Hf}/^{177}\text{Hf}$	$\pm 2\sigma$	$^{176}\text{Hf}/^{177}\text{Hf}_{\text{fi}}$	$\epsilon\text{Hf(t)}$	T_{DM1} (Ma)	T_{DM2} (Ma)
YB15-08	600	0.0167	1.9E-04	0.000454	4.5E-06	0.282011	1.2E-05	0.282006	-14.17	1720	2409
YB15-09	600	0.0168	2.0E-04	0.000458	4.8E-06	0.282033	1.2E-05	0.282028	-13.41	1691	2361
YB15-10	600	0.0216	1.7E-04	0.000577	4.8E-06	0.282011	1.2E-05	0.282005	-14.23	1726	2412

$$\text{Hf}_i = \left(\frac{(^{176}\text{Hf})_S - ((^{176}\text{Lu})_S / (^{177}\text{Hf})_S)^{(\lambda * t)}}{((^{176}\text{Lu})_S / (^{177}\text{Hf})_S)^{(\lambda * t)} - 1) \right) * 10000.$$

$$T_{\text{DM1}} = \left(\frac{1}{\lambda} * \ln(1 + ((^{176}\text{Hf})_S - ((^{176}\text{Lu})_S / (^{177}\text{Hf})_S)^{(\lambda * t)}) / ((^{176}\text{Lu})_S / (^{177}\text{Hf})_S)) \right) / ((^{176}\text{Hf})_{\text{CHUR},0} - ((^{176}\text{Lu})_{\text{CHUR},0} / (^{177}\text{Hf})_{\text{CHUR},0})^{(\lambda * t)})$$

$$T_{\text{DM2}} = T_{\text{DM1}} * (T_{\text{DM1}} * t / 1000) * ((f_{\text{CC}} - ((^{176}\text{Lu})_S / (^{177}\text{Hf})_{\text{CHUR},0})^{(\lambda * t)}) / (f_{\text{CC}} * f_{\text{DM}})).$$

f_{DM2} have been adopted as stage model.

($^{176}\text{Hf}/^{177}\text{Hf}$)_S, ($^{176}\text{Lu}/^{177}\text{Hf}$)_S measured values; ($^{176}\text{Lu}/^{177}\text{Hf}$)_{CHUR} = 0.0336 ± 1, ($^{176}\text{Hf}/^{177}\text{Hf}$)_{CHUR} = 0.282785 ± 11 (Bouvier et al., 2008).

($^{176}\text{Lu}/^{177}\text{Hf}$)_{DM} = 0.0384, ($^{176}\text{Hf}/^{177}\text{Hf}$)_{DM} = 0.28325 (Griffin et al. 2000).

$f_{\text{CC}} = -0.548$ (composition of continental crust), $f_{\text{DM}} = 0.16$; $\lambda = 1.867 \times 10^{-11}$ year⁻¹ calculations based on (Söderlund et al. 2004), t = intrusion age.

Table 4

Whole rock silica contents (wt.%), and calculated $\delta^{18}\text{O}$ (whole rock) (calculated after Valley et al., 1994).

Sample	Rock type	$\delta^{18}\text{O}$ (zircon)	SiO ₂ (wt.%)	$\delta^{18}\text{O}$ (WR) (calc.)
YB21	syenite	6.26	61.7	7.53
Y18	monzonite	6.81	52.1	7.50
YB8	syenite	7.21	62.5	8.53
YB15	syenite	6.57	61.0	7.80

grains) following empirical $\delta^{18}\text{O}_{\text{Zrn}}$ versus SiO₂ correlation (whole rock) (Valley et al., 1994). The results are 7.5‰ for samples YB21 and Y18, and 8.5‰ and 7.8‰ for samples YB8 and YB15, respectively.

5.4. Whole-rock major and trace elements geochemistry

The syenite samples have SiO₂ content between 58.8 and 65.8 wt% (Table 5) while monzonite samples are comparatively less siliceous (SiO₂ = 52.1 to 56.3 wt%). The rocks show high HFSE (Zr + Nb + Ce + Y = 380 to 1043 ppm), total Rare Earth Element abundance (ΣREE from 182 to 511 ppm), and moderate to high (Na₂O + K₂O)/CaO ratio (1.5–8.0), moderate to high 10,000 * Ga/Al ratio (2.3 to 3.4), moderate to high Nb (11.6–62.6 ppm), Zr (245–810 ppm) and Hf (5.8–18.3 ppm) contents. In the total alkali - silica (TAS) classification diagram, they plot in the syenite and monzonite fields (Fig. 7a). All the samples show high alkali contents (K₂O + Na₂O = 8.0–12.5 wt%) and > 1 K₂O/Na₂O ratio (1.3 and 2.2). They have higher abundances of LILE, such as Ba (1522–3664 ppm), Sr (640–1553 ppm), Rb (157–326 ppm), etc. They display alkali nature in the SiO₂ wt.% versus (Na₂O + K₂O - CaO) modified alkali lime index diagram of Frost et al. (2001) (Fig. 7b) while their moderate Fe[#] (Fe[#] = [FeO/(FeO + MgO)]) values (0.5–0.7), underline a magnesian affinity and I-type granitoid characteristics (Frost et al., 2001) (Fig. 7c). In the Shand's molar Al₂O₃/(CaO + Na₂O + K₂O) vs. Al₂O₃/(Na₂O + K₂O) diagram the rocks define a metaluminous character (Maniar and Piccoli, 1989) (Fig. 7d), and their A/CNK < 1.1 values further conform to the I-type origin (Chappell and White 1992). They display shoshonitic affinity in Ta/Yb vs. Th/Yb classification diagram of Müller et al. (1992) and SiO₂ vs. K₂O diagram of Peccerillo and Taylor (1976) (Fig. 7e, f).

In the bivariate plots TiO₂, MgO, CaO, P₂O₅ and Fe₂O₃, display a general decrease with increasing SiO₂ while Al₂O₃, Na₂O and K₂O, display a general covariance with SiO₂ (Fig. 8). Although the relationships are nonlinear, they suggest fractional crystallization as the main process of magma evolution.

The Chondrite-normalized REE patterns show LREE enrichment, seen as moderately steep LREE to MREE trend and (La/Yb)_N ratios between 18.1 and 41.7 with moderate to pronounced positive Eu anomalies (Eu/Eu^{*} = 0.4–2.3) (Fig. 9a). A general overlap in the chondrite normalized patterns implies that the different magma emplacements likely originated from geochemically close sources.

In the primitive mantle (PM)-normalized spiderdiagrams (Fig. 9b), these rocks show spikes for large ion lithophile elements (LILEs, such as Cs, Rb, Ba and Sr), HFSEs (such as Th and U) and LREEs, with a striking positive Pb anomaly, and pronounced Nb-Ta and Ti depletion.

5.5. Whole rock Sr-Nd isotopic data

Whole-rock Sr-Nd isotopic compositions of five syenite and one monzonite samples are listed in Table 6. The initial $^{87}\text{Sr}/^{86}\text{Sr}$ ratios ($^{87}\text{Sr}/^{86}\text{Sr}$)_i and $\epsilon\text{Nd(t)}$ values were back-calculated using the crystallization ages of ca. 660, 630 and 600 Ma and assuming an age of ca. 630 and 600 Ma for samples YB19 and YB6 (due to their geographical proximity with the samples Y18 and YB8), respectively. The ca. 660 Ma (YB21) sample shows high Rb/Sr and ($^{87}\text{Sr}/^{86}\text{Sr}$)_i values of 0.20 and 0.705197. These values are 0.17–0.28 and 0.705695–0.706448 for the samples crystallized and assumed crystallized at ca. 630 Ma (Y18 and

YB19). For the ca. 600 Ma samples the corresponding values range between 0.25 and 0.33, and 0.705818 and 0.706499, respectively. The ca. 660 Ma, 630 Ma and 600 Ma samples also display $\epsilon\text{Nd(t)}$ values of −8.8, −8.1 to −9.4 and −9.0 to −10.0, respectively (Fig. 10a) with Paleoproterozoic model ages (T_{DM}) of 1913, 1691–1807 and 1787–1886 Ma (Table 6). In the ($^{87}\text{Sr}/^{86}\text{Sr}$)_i vs. $\epsilon\text{Nd(t)}$ diagram, rocks from the Linte massif plot close to the majority of the Bafoussam shoshonitic granitoids (Djouka Fonkwe et al., 2008) and the Kekem shoshonitic gabbro-norite (Kwékam et al., 2013) (Fig. 10a), approximately 200 km to the west of the Linte massif.

6. Discussion

6.1. Geochronology

Zircon U-Pb data from the Linte massif show evidence of Paleoproterozoic and Neoproterozoic magmatism in the Adamawa-Yade domain. A single inherited zircon in monzonite sample Y18 yielded a 1983 Ma age, and an upper intercept age of 2064 ± 41 Ma in syenite sample YB21 testifies the involvement of reworked Paleoproterozoic crustal material in producing the Neoproterozoic Linte magmas. Within uncertainty, the 2064 ± 41 Ma age can be correlated with 2069 ± 12 Ma, 2073 ± 13 Ma and 2081 ± 26 Ma, magmatic events reported for Maham dioritic orthogneisses, and the Makénéné and Nomalé migmatites (Tchakounté et al., 2017) located ca. 100 km to the west and southwest of the Linte area, in the western part of the Adamawa-Yade domain. Paleoproterozoic inherited zircons have also been reported from Mbé (2104 ± 7 Ma, Penaye et al., 1989) and Buffle Noir (2130 ± 20 Ma, Toteu et al., 2001) regions in the northern part of the Adamawa-Yade domain (e.g., Toteu et al., 2001). $^{207}\text{Pb}/^{206}\text{Pb}$ ages of ~2000 Ma (1685 ± 4 Ma to 2388 ± 5 Ma, Ganwa et al., 2008) have been reported from the eastern part of the Adamawa-Yade domain in the Meiganga region. Paleoproterozoic crystallization ages have been reported in the northwestern corner of the Congo Craton, in south western Cameroon (e.g., 2055 ± 5 Ma and 2066 ± 4 Ma, Lerouge et al., 2006). $^{207}\text{Pb}/^{206}\text{Pb}$ ages of 1895 ± 14 and 2060 ± 23 Ma (Silva Filho et al., 2010) have been also reported from inherited zircon cores in the Ediacaran syenogranites of the Aguas Belas pluton in the Pernambuco-Alagoas crustal domain (PEAL) (Van Schmus et al., 2008) of the Brasiliano Pan-African orogeny in northeastern Brazil.

Field observations (Fig. 1c) show a clear sequence of intrusion in the Linte syenite massif. The oldest medium-grained rocks were expected to occur closer to the rim of the massif, because the cooling and the crystallization of magma should begin at the rim of the massif and should be faster due to contrast of temperature with enclosing rocks. And consequently, the younger coarse-grained rocks should occur at the central part. However, the four U-Pb zircon ages (YB21 - ca. 660 Ma, Y18 - ca. 630 Ma, YB8 and YB15 - ca. 600 Ma) and the sequence of intrusion wherein the coarse-grained rocks (e.g., Y18 and YB15) occur at the rim and the medium-grained ones (e.g., YB21 and YB8) in the central part of the Linte syenite massif, are inconsistent with this assertion. This could be due to either different magma sources or protracted magma emplacement. The oldest U-Pb ages obtained in samples YB21 and Y18, may not represent a 660 Ma and 630 Ma magmatic crystallization but could be a result of partial Pb loss (of the ca. 2000 Ma inherited grains). This assumption can be verified through the zircon Lu-Hf isotope system (e.g., Gerdes and Zeh, 2009; Zeh et al., 2009, 2010). The zircon grains dated to ca. 660 and 630 Ma show similar initial $^{176}\text{Hf}/^{177}\text{Hf}$ ratios of 0.282061 to 0.282476 (average = 0.282356), which are different from the initial $^{176}\text{Hf}/^{177}\text{Hf}$ ratios of 0.281097 to 0.281444 (average = 0.281153) of the ca. 2000 Ma inherited zircon grains. This implies that, the ca. 660 and 630 Ma zircon grains did not result from Pb loss of Paleoproterozoic zircon grains, nor related to these latters. Further, the ca. 660 and 630 Ma zircon grains have Mesoproterozoic to Paleoproterozoic Hf-T_{DM2} ages of ca. 1300–2300 Ma, which are different to Archean Hf-T_{DM2} ages of ca. 2800–3500 Ma show by the ca. 2000 Ma

Table 5

Major (in wt. %) and trace (in ppm) element data of the Linte syenitic massif.

	Syenite														Monzonite											
	Y7	Y8	Y9	Y10	Y11	Y14	Y16	Y17	YB1	YB6	YB7	YB8	YB11	YB12	YB13	YB13'	YB15	YB19	YB20	YB21	YB22	YBS1	Y13	Y13'	Y18	YB10
Major elements (wt.%)																										
SiO ₂	61.9	64.4	62.6	62.7	64.1	58.8	60.5	60.9	59.3	62.0	60.8	62.5	59.1	61.6	60.6	60.6	61.0	63.8	65.8	61.7	61.2	60.5	56.3	56.1	52.1	55.5
TiO ₂	0.55	0.52	0.41	0.57	0.66	0.99	0.71	0.52	0.93	0.69	0.71	0.65	0.82	0.57	0.71	0.71	0.78	0.36	0.59	0.41	0.65	0.74	0.94	0.95	1.13	0.90
Al ₂ O ₃	16.8	14.9	16.7	16.5	15.8	15.1	15.6	17.4	14.5	16.1	16.2	15.5	15.2	17.0	16.6	16.5	17.5	17.9	15.1	16.2	16.9	16.1	15.8	15.9	11.9	11.3
Fe ₂ O ₃	3.86	3.52	2.97	3.53	3.27	5.57	4.24	3.42	5.16	3.81	4.29	3.88	4.97	3.45	4.11	4.11	2.76	2.11	3.12	3.59	3.69	4.37	5.48	5.42	7.46	7.90
MnO	0.05	0.05	0.04	0.05	0.05	0.09	0.07	0.05	0.08	0.06	0.05	0.07	0.07	0.06	0.07	0.07	0.04	0.03	0.05	0.05	0.05	0.07	0.08	0.08	0.12	0.14
MgO	2.03	2.28	2.15	1.72	1.70	3.92	3.29	1.98	4.05	2.29	2.38	2.42	3.96	1.99	2.55	2.56	2.08	0.86	1.64	2.59	2.05	2.76	3.80	3.82	7.04	6.92
CaO	2.26	2.06	2.18	1.96	1.76	3.71	2.79	2.20	3.29	2.25	2.30	2.16	3.44	1.89	2.44	2.43	1.69	1.41	1.48	2.01	2.03	2.53	5.25	5.23	4.73	5.35
Na ₂ O	4.28	3.83	4.08	4.13	4.53	4.10	3.80	4.49	4.16	4.50	4.26	4.02	3.64	4.75	4.82	4.78	4.28	4.60	4.61	3.92	4.36	4.66	2.88	2.93	2.59	2.63
K ₂ O	6.56	6.68	6.71	6.90	6.14	5.64	5.84	7.42	6.53	6.47	7.13	7.08	6.66	6.69	6.28	6.19	8.18	6.71	6.28	7.44	7.14	6.32	6.35	6.36	5.46	5.43
P ₂ O ₅	0.32	0.36	0.31	0.32	0.22	0.53	0.45	0.37	0.51	0.35	0.40	0.42	0.62	0.34	0.36	0.36	0.29	0.15	0.28	0.42	0.38	0.38	0.60	0.60	0.81	0.99
LOI	0.45	0.79	0.52	0.49	0.65	1.04	2.39	0.49	0.83	0.36	0.69	0.95	0.88	0.85	0.78	0.74	0.72	0.51	0.73	0.57	0.39	0.39	1.45	1.59	5.95	0.75
TOL	99.1	99.4	98.7	98.8	99.4	99.6	99.2	99.3	98.9	99.1	99.7	99.4	99.2	99.3	99.1	99.3	98.4	99.7	98.9	98.8	98.8	98.9	99.0	99.2	97.9	
(Na ₂ O + K ₂ O)/CaO	4.79	5.12	4.95	5.61	6.05	2.62	3.45	5.42	3.25	4.88	4.95	5.15	2.99	6.04	4.55	4.51	7.37	8.03	7.37	5.64	5.67	4.33	1.76	1.78	1.70	1.51
K ₂ O + Na ₂ O	10.8	10.5	10.8	11.0	10.7	9.7	9.6	11.9	10.7	11.0	11.4	11.1	10.3	11.4	11.1	11.0	12.5	11.3	10.9	11.4	11.5	11.0	9.2	9.3	8.0	8.1
K ₂ O/Na ₂ O	1.53	1.74	1.64	1.67	1.36	1.38	1.54	1.65	1.57	1.44	1.67	1.76	1.83	1.41	1.30	1.29	1.91	1.46	1.36	1.90	1.64	1.36	2.20	2.17	2.11	2.06
A/NK	1.19	1.10	1.20	1.16	1.12	1.17	1.24	1.13	1.04	1.12	1.10	1.09	1.15	1.13	1.13	1.14	1.10	1.21	1.05	1.04	1.13	1.11	1.36	1.36	1.17	1.11
A/CNK	0.92	0.86	0.93	0.93	0.91	0.77	0.88	0.89	0.73	0.87	0.86	0.85	0.78	0.92	0.87	0.87	0.92	1.03	0.89	0.73	0.91	0.84	0.75	0.75	0.63	0.57
FeO	3.47	3.16	2.67	3.18	2.94	5.01	3.81	3.08	4.64	3.42	3.86	3.49	4.47	3.10	3.69	3.69	2.48	1.89	2.80	3.23	3.32	3.93	4.93	4.88	6.71	7.10
Fe#	0.63	0.58	0.55	0.65	0.63	0.56	0.54	0.61	0.53	0.60	0.62	0.59	0.53	0.61	0.59	0.59	0.54	0.69	0.63	0.55	0.62	0.59	0.57	0.56	0.49	0.51
Trace elements (ppm)																										
Li	16.1	22.5	21.1	17.2	53.7	6.24	9.52	1.66	61.8	32.4	21.4	34.1	35.4	21.9	37.7		25.0	9.00	39.1	14.9	16.8	43.4	10.4	37.1	54.8	
Be	3.91	7.85	8.77	6.51	16.7	16.9	4.15	4.69	14.8	11.3	7.06	10.5	6.90	5.99	11.6		8.05	6.83	15.1	2.57	5.6	21.5	7.22	10.5	8.69	
Sc	8.22	8.42	7.04	7.04	6.69	13	9.39	6.59	11.1	7.73	9.23	8.48	11.7	7.04	8.58		5.71	3.63	5.93	7.21	7.27	9.97	11.9	17.7	20.7	
V	72.3	69.9	64.8	64.8	56.1	132	92.5	54	116	86.6	88.8	72.3	111	53.2	78.0		67.3	38.0	54.6	83.9	70.9	94.2	148	157	177	
Cr	84.9	118	93.7	55.9	80.0	193	125	69.2	179	97.4	91.0	98.8	164	67.0	113		84.0	23.1	66.9	112	71.1	128	158	335	343	
Co	11.3	135	112	75.2	128	56.9	50.7	87.9	56.5	114	93.9	72.4	113	88.5	79.1		85.4	90.7	128	83.4	109	12.6	103	52.3	90.1	
Ni	28.9	58.8	52.1	31.1	40.5	83.4	56.2	42.1	82.9	48.3	48.9	54.4	96.4	53.9	47.2		52.1	19.3	40.2	60.9	54.3	50.1	84.1	149	141	
Cu	33.0	27.1	10.3	31.2	42.2	130.0	61.6	12.2	54.5	77.3	37.0	38.3	64.5	39.1	54.5		85.5	8.0	11.1	29.9	48.8	22.8	58.0	27.9	61.8	
Zn	69.8	57.2	45.1	59.5	62.1	100	67.9	56.6	82.4	60.4	52.7	66.7	75.5	59.2	72.8		44.4	35.3	47.7	43.9	67.9	76.4	89.8	120	139	
Ga	22.2	23.1	20.8	22.7	26.9	24.8	22.4	21.6	24.9	24.7	23.1	23.6	23.2	24.9	25.0		24.8	23.3	23.7	20.7	23.6	27.6	24.2	20.5	20.6	
Rb	161	281	220	227	310	235	157	205	310	277	248	323	244	217	240		326	228	269	257	223	287	190	298	285	
Sr	1123	913	1191	1148	654	1116	1100	1433	1081	1029	844	966	1553	942	1065		1300	1330	640	1286	1176	981	1150	1061	833	
Y	22.0	20.3	26.3	17.7	20.9	30.0	16.6	15.5	22.9	18.3	18.4	21.9	23.7	17.0	29.0		12.9	11.7	26.6	18.3	22.9	21.7	23.7	31.3	38.9	
Zr	369	406	301	318	810	785	527	245	521	518	546	370	352	577	702		311	282	453	258	518	622	757	377	291	
Nb	17.9	26.2	14.8	19	62.6	52.8	18.9	14.6	45.3	35.6	27.3	33.9	22.1	20.1	45.8		33.4	14.1	30.5	11.6	34.4	49.6	18.7	36.1	26.4	
Mo	0.66	1.16	1.19	1.32	3.45	0.46	0.46	0.61	1.14	0.83	1.13	0.86	0.71	1.73	2.60		2.90	0.69	1.88	0.69	2.26	2.39	0.43	1.8	0.57	
Syenite																										
	Y7	Y8	Y9	Y10	Y11	Y14	Y16	Y17	YB1	YB6	YB7	YB8	YB11	YB12	YB13	YB13'	YB15	YB19	YB20	YB21	YB22	YBS1	Y13	Y13'	Y18	YB10
Trace elements (ppm)																										
Sn	2.57	3.17	1.62	2.4	3.56	4.38	1.79	1.94	4.39	3.41	3.68	3.41	2.64	2.52	4.34		2.52	1.53	3.49	1.87	3.64	4.76	1.83	3.38	4.50	
Cs	3.98	5.09	9.18	4.82	11.1	1.48	1.01	1.65	14.1	10.1	5.09	8.77	5.33	4.32	4.57		7.75	4.25	9.65	2.81	2.02	7.31	1.11	14.1	9.98	
Ba	2509	2236	2436	2675	1522	2220	2911	3442	2548	2368	2128	2367	3664	2328	2595		3424	2428	1615	3064	2722	2231	3420	2071	1986	
La	66.5	78.6	49.3	68.8	81.7	99.1	59.7	60.8	87.4	69.8	74	90.7	84.3	63.2	99.9		50	48.9	104	64.9	85.4	79.3	87.1			

Table 5 (continued)

	Syenite													Monzonite											
	Y7	Y8	Y9	Y10	Y11	Y14	Y16	Y17	YB1	YB6	YB7	YB8	YB11	YB12	YB13	YB13'	YB15	YB19	YB20	YB21	YB22	YBS1	Y13	Y13'	Y18
Dy	4.03	3.66	3.38	2.97	3.55	4.94	3.01	2.86	4.17	3.08	3.37	3.80	4.13	3.06	5.30	2.18	1.50	4.51	3.26	3.96	3.78	4.37	5.71	6.77	
Ho	0.71	0.68	0.71	0.57	0.69	0.97	0.56	0.49	0.76	0.59	0.59	0.71	0.78	0.57	1.00	0.42	0.32	0.81	0.58	0.72	0.72	0.78	1.06	1.22	
Er	1.71	1.68	1.96	1.40	1.86	2.48	1.37	1.19	2.00	1.51	1.55	1.76	1.92	1.50	2.56	1.08	0.91	2.09	1.53	1.93	1.86	2.03	2.69	3.06	
Tm	0.23	0.24	0.29	0.22	0.29	0.37	0.22	0.18	0.32	0.24	0.23	0.27	0.27	0.23	0.36	0.17	0.15	0.28	0.22	0.28	0.29	0.27	0.42	0.44	
Yb	1.39	1.51	1.95	1.36	1.88	2.40	1.41	1.09	1.94	1.53	1.43	1.72	1.81	1.33	2.39	0.99	0.97	1.79	1.38	1.83	1.86	1.66	2.55	2.65	
Lu	0.22	0.23	0.33	0.21	0.30	0.34	0.20	0.16	0.30	0.25	0.24	0.25	0.27	0.21	0.35	0.15	0.16	0.28	0.20	0.26	0.27	0.23	0.39	0.41	
Hf	8.48	9.68	7.16	7.67	18.3	16.2	10.7	5.79	11.0	11.1	12.8	8.86	7.49	13.0	14.3	7.17	7.44	10.7	5.82	11.7	13.0	14.94	8.49	7.36	
Ta	0.69	1.73	1.57	1.24	3.06	2.61	0.94	0.95	2.22	2.07	1.36	2.06	1.36	0.92	2.31	1.86	1.10	1.31	0.55	2.41	2.48	0.68	1.87	1.34	
Pb	40.5	44.2	56.0	47.1	70.1	56.1	45.9	34.4	75.5	74.4	54.1	60.2	57.0	62.3	85.6	62.8	44.7	76.5	41.8	49.8	78.6	47.1	45.5	34.3	
Bi	0.06	0.11	0.16	0.09	0.12	0.18	0.08	0.04	0.07	0.12	0.07	0.11	0.09	0.06	0.08	0.06	0.05	0.09	0.05	0.03	0.13	0.13	0.04	0.09	
Th	10.1	48.4	16.4	22.9	75.8	28.3	5.9	17.4	40.1	39.4	43.2	33.5	22.7	17.3	17.4	27.0	22.7	38.2	7.09	34.5	56.6	8.52	19.5	22.8	
U	2.58	7.07	5.72	5.80	7.17	5.33	1.53	3.03	6.87	4.74	3.35	4.45	3.48	4.12	3.09	5.79	5.06	8.08	1.90	4.44	8.79	2.09	4.31	5.46	
Σ REE	258	306	200	262	305	396	237	241	340	277	272	347	341	263	347	192	182	380	248	342	312	346	438	511	
(La/Yb)N	34.4	37.2	18.1	36.2	31.2	29.6	30.4	40.0	32.2	32.7	37.1	37.8	33.3	34.1	29.9	36.4	36.0	41.7	33.6	33.4	30.6	37.6	29.5	33.6	
Eu/Eu*	0.54	0.68	1.24	0.99	0.54	0.61	1.17	1.26	0.67	1.03	1.06	0.72	1.00	0.89	0.96	1.72	2.27	0.37	1.08	0.74	0.70	1.01	0.50	0.47	
Rb/Sr	0.14	0.31	0.18	0.20	0.47	0.21	0.14	0.14	0.29	0.27	0.29	0.33	0.16	0.23	0.23	0.25	0.17	0.42	0.20	0.19	0.29	0.17	0.28	0.34	
Th/U	3.91	6.85	2.87	3.95	10.57	5.31	3.82	5.74	5.84	8.31	12.90	7.53	6.52	4.20	5.63	4.66	4.49	4.73	3.73	7.77	6.44	4.07	4.52	4.18	
Th/La	0.15	0.62	0.33	0.33	0.93	0.29	0.10	0.29	0.46	0.56	0.58	0.37	0.27	0.27	0.17	0.54	0.46	0.37	0.11	0.40	0.71	0.10	0.19	0.18	
Nb/U	6.94	3.71	2.59	3.28	8.73	9.91	12.35	4.82	6.59	7.51	8.15	7.62	6.35	4.88	14.8	5.77	2.78	3.77	6.11	7.75	5.64	8.94	8.38	4.84	
Ta/U	0.27	0.24	0.27	0.21	0.43	0.49	0.61	0.31	0.32	0.44	0.41	0.46	0.39	0.22	0.75	0.32	0.22	0.16	0.29	0.54	0.28	0.33	0.43	0.25	
Ce/Pb	2.57	3.10	1.44	2.48	2.01	3.12	2.22	3.05	2.03	1.73	2.07	2.56	2.65	1.94	1.58	1.37	1.90	2.01	2.49	3.13	1.81	3.25	4.31	6.47	
Lu/Hf	0.03	0.02	0.05	0.03	0.02	0.02	0.03	0.03	0.02	0.02	0.02	0.03	0.04	0.02	0.02	0.02	0.02	0.03	0.03	0.02	0.02	0.02	0.05	0.06	
Zr + Nb + Ce + Y	513	590	423	472	1035	1043	665	380	742	701	704	580	549	735	912	443	393	664	392	731	835	953	640	578	
10000 ^a Ga/Al	2.50	2.92	2.35	2.60	3.23	3.11	2.72	2.35	3.26	2.90	2.70	2.87	2.88	2.76	2.84	2.68	2.46	2.96	2.42	2.64	3.23	2.89	3.25	3.44	
T _{Zr} (°C)	873	881	856	863	967	909	897	830	864	903	904	867	833	924	932	861	867	904	836	909	914	879	769	735	

Note: FeO = Fe₂O₃*0.8998; Fe# = FeO/(FeO + MgO); LOI: loss on ignition; A/CNK molar = Al₂O₃/(CaO + Na₂O + K₂O); A/NK molar = Al₂O₃/(Na₂O + K₂O).

Subscript N = chondrite-normalized value from Sun and McDonough (1989). T_{Zr}: zircon saturation temperature (after Watson and Harrison (1983)).

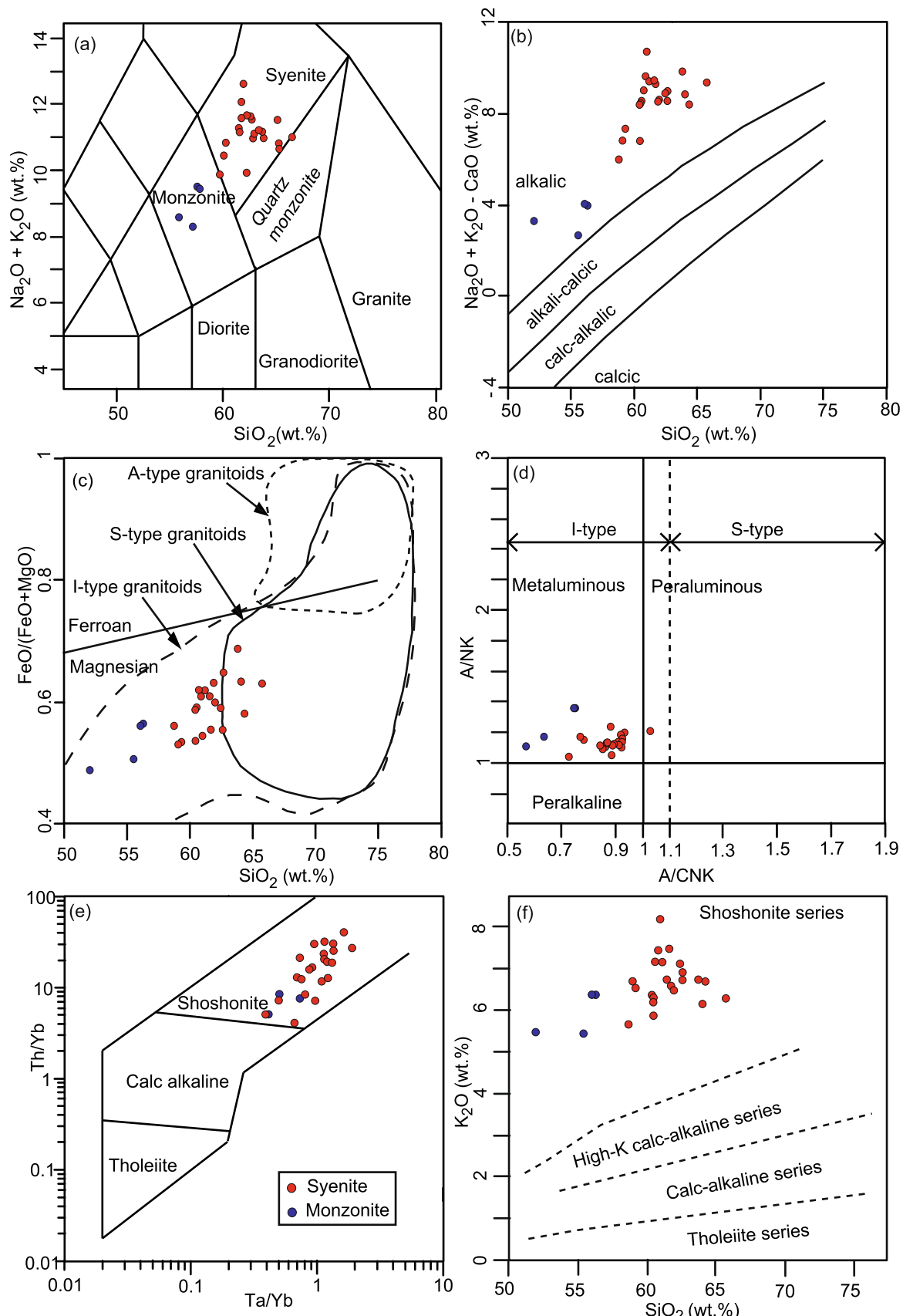


Fig. 7. Geochemical classification of the rocks from the Linte massif. (a) Silica (wt.%) vs. total alkali ($\text{Na}_2\text{O} + \text{K}_2\text{O}$) (wt.%) (Middlemost, 1994). (b) silica (wt.%) vs. $(\text{Na}_2\text{O} + \text{K}_2\text{O}) - \text{CaO}$ (wt.%) (Frost et al., 2001). (c) Silica (wt.%) vs. $\text{FeO}/(\text{FeO} + \text{MgO})$ (Frost et al., 2001). (d) Shand's index molar $\text{Al}_2\text{O}_3/(\text{CaO} + \text{Na}_2\text{O} + \text{K}_2\text{O})$ vs. $\text{Al}_2\text{O}_3/(\text{Na}_2\text{O} + \text{K}_2\text{O})$ diagram (after Maniar and Piccoli, 1989). (e) Ta/Yb vs. Th/Yb (Müller et al., 1992). (f) Silica (wt.%) vs. K_2O (wt.%) (Peccerillo and Taylor, 1976).

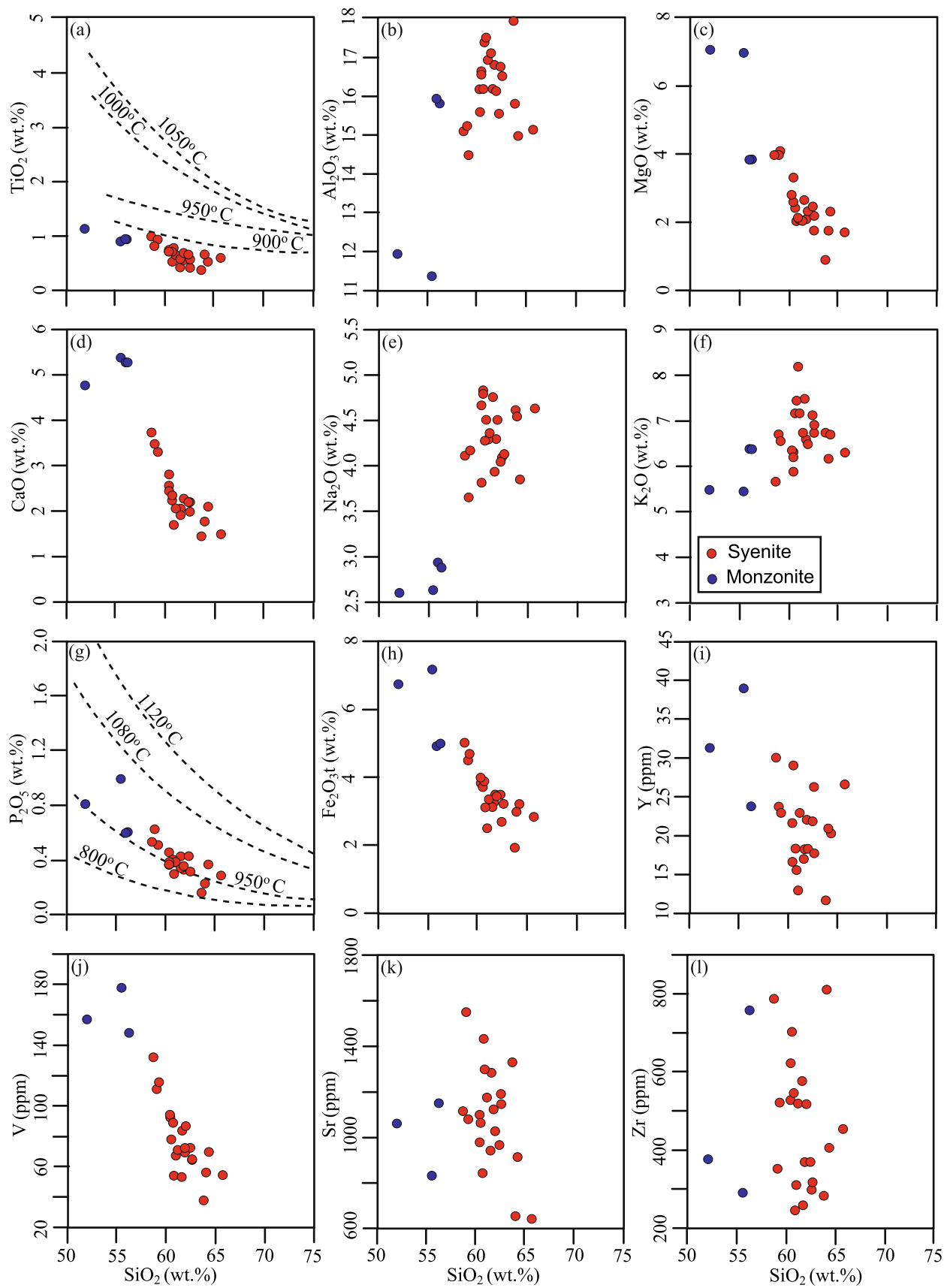


Fig. 8. Selected silica (wt.%) vs. major (wt.%) and vs. trace elements (ppm) diagrams for rocks from the Linde massif. Isotherms in (a) and (g) are from Green and Pearson (1986) and Green and Watson (1982). (For interpretation of the references to colour in this figure legend, the reader is referred to the web version of this article.)

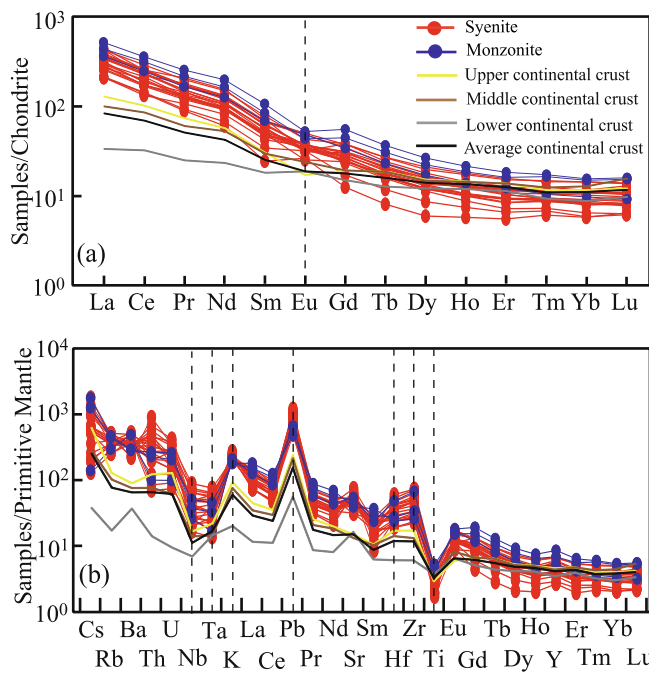


Fig. 9. (a) Chondrite-normalized REE and (b) Primitive Mantle-normalized trace element patterns for the rocks from the Linte massif. The upper, middle, lower and average continental crust values are from Rudnick and Gao (2003), and the Chondrite and the Primitive Mantle normalizing values are from Sun and McDonough (1989).

inherited zircon grains (Table 3). Therefore, the samples YB21 and Y18 and the respective ages at ca. 660 and 630 Ma are not considered to be related to the Paleoproterozoic crustal material (ca. 2000 Ma), but rather considered to be part of rocks and the crystallization time of the Linte massif. The initial $^{176}\text{Hf}/^{177}\text{Hf}$ ratios of ca. 600 Ma zircon grains are quite distinct (0.281992–0.282097; average = 0.282045) from the two precedent ratio groups (at ca. 2000 Ma and ca. 660–630 Ma). Therefore, the Pan-African crystallization age of the Linte massif is established by the measured ages between ca. 660 and 600 Ma, indicating a protracted magmatism spanning at least 60 Ma underlining a temporal transition from west to east. The crystallization at 662 ± 4 Ma corresponds to ages reported in the north and the south of the Adamawa-Yade domain, respectively for metagranodiorites (665 ± 10 Ma, Toteu et al., 2006b) in the Poli region and for metagabbros (666 ± 26 Ma, Toteu et al., 2006a) in the southeast of Lomié. The crystallization at 633 ± 3 Ma corresponds with Bapé orthogneisses (628 ± 3 , Tchakounté et al., 2017), Tonga synkinematic granitoid (618 ± 20 Ma, Njiosseu et al., 2005), Bangwa metaleucogranite and metagranodiorite (638 ± 2 and 637 ± 5 Ma, Njiekak et al., 2008), Bapa-Batié biotite granite (619 ± 19 Ma; Chebeu et al., 2011), Meiganga dioritic protolith (637 ± 5 , Ganwa et al., 2018) and the Landou granite (632 ± 13 Ma, Nomo et al., 2017) in western Cameroon and west, east and north of the Adamawa-

Yade domain. The 633 ± 3 Ma is also close to the crystallization ages of syenitic rocks (632 ± 5 , Silva Filho et al., 2016) of the Serra do Catú Suite in the PEAL domain in NE Brazil. The crystallization at 603 ± 4 and 600 ± 3 Ma possibly marks the culmination of magmatism in the Linte syenitic massif. These ages compare well with events in the west Cameroon in the Batié porphyrogranite (602 ± 1.4 Ma, Njiekak et al., 2008), the Bapa-Batié biotite-amphibole granite (600 ± 3.7 Ma, Chebeu et al., 2011) and in the east of the Adamawa-Yade in the Meiganga amphibole biotite granite (601 ± 1 Ma zircon evaporation age, Ganwa, 2005; Ganwa et al., 2011). The ca. 600 Ma event is also in agreement with 591 ± 19 and 590 ± 20 Ma (e.g., Toteu et al., 1994; Lerouge et al., 2006) magmatism in the northwestern segment of the Congo Craton cover, in the Rocher du Loup metasyenites. Rocks of the Brasiliense orogen also have similar ages reported from the Correntes pluton in the PEAL domain (602 ± 5 Ma, Silva Filho et al., 2016). The Umarizal igneous association of the Borborema Province has been dated to 592.6 ± 5 Ma (McReath et al., 2002); and 610 ± 4 to 612 ± 7 Ma ages have been obtained from the Água Branca suite and the Mata Grande Pluton, respectively, in the PEAL domain (Silva Filho et al., 2016).

6.2. Effects of alteration

The studied rocks do not show significant mesoscale deformations features despite development of foliation and gneissic structure within the surrounding orthogneisses and granitoids. The microscale observations, such as undulose extinction, chessboard microstructure, myrmekite, recrystallizations, microclinization of orthoclase, deformed twinning in plagioclase and bent cleavage in biotite, etc. indicate some deformation and metamorphism. High LOI values (2.4 and 5.9 wt%, respectively for syenite and monzonite), coupled with chloritization and sericitization, suggest alteration and metasomatism.

Zr generally remains immobile during metamorphism and alteration processes, and can be considered as an alteration-independent index in geochemical data evaluation (Pearce and Peate, 1995; Wang et al., 2018). TiO_2 , Fe_2O_3 (transition elements), Sr (LILE), Sm, Nd (REE), Hf and Y (HFSE) vs. Zr diagrams for the Linte rocks show sub-linear correlations (Fig. 11a-g), indicating that these elements more or less preserved their pristine content. The similarities in REE and HFSE patterns, in the chondrite-normalized REE (Fig. 9a) and the PM-normalized multi-element spider diagrams (Fig. 9b) further support an overall immobility of these elements. Therefore, REE, HFSE, some LILE and transition elements have been used for discussion and interpretation.

6.3. Magmatic evolution: Fractional crystallization

Syenites and monzonites have similar Nd isotopic signatures (Fig. 10a) despite being emplaced at different times, and their major and trace element characteristics indicate crystal fractionation as a dominant magma evolution process (Fig. 8). Their $\epsilon\text{Nd(t)}$ values lack a systematic correlation with increasing of Nb/La ratios (Fig. 10b) and SiO_2 contents (Fig. 10c), further suggesting fractional crystallization as the major magma differentiation process. This is also apparent from the negative (TiO_2 , MgO , CaO , P_2O_5 , Fe_2O_3 , Y, V, Sr and Zr) and positive

Table 6
Sr and Nd isotope data of samples from the Linte syenitic massif.

Sample	Rock type	U-Pb age Ma	Rb (ppm)	Sr (ppm)	Rb/ Sr	$^{87}\text{Sr}/^{86}\text{Sr}$	$^{87}\text{Rb}/^{86}\text{Sr}^*$	$^{87}\text{Sr}/^{86}\text{Sr}$	Sm (ppm)	Nd (ppm)	$^{147}\text{Sm}/^{144}\text{Nd}^*$	$^{143}\text{Nd}/^{144}\text{Nd}$	ϵNd (t)	TDM (Ga)
YB21	syenite	662	257	1286	0.20	0.710666	0.5790	0.705197	7.69	44.1	0.1054	0.511789	-8.75	1913
Y18	monzonite	633	298	1061	0.28	0.713032	0.8126	0.705695	13.1	77.5	0.1019	0.511823	-8.14	1807
YB19	syenite	633	228	1330	0.17	0.710917	0.4950	0.706448	3.70	27.9	0.0801	0.511666	-9.44	1691
YB6	syenite	603	277	1029	0.27	0.713195	0.7786	0.706499	7.30	44.2	0.0998	0.511739	-9.98	1886
YB8	syenite	603	323	966	0.33	0.714135	0.9672	0.705818	9.31	59.0	0.0953	0.51176	-9.22	1787
YB15	syenite	600	326	1300	0.25	0.712423	0.7254	0.706216	5.17	31.1	0.1003	0.511794	-8.98	1820

* $^{87}\text{Rb}/^{86}\text{Sr}$ and $^{147}\text{Sm}/^{144}\text{Nd}$ ratios were calculated from elemental data measured by ICPMS.

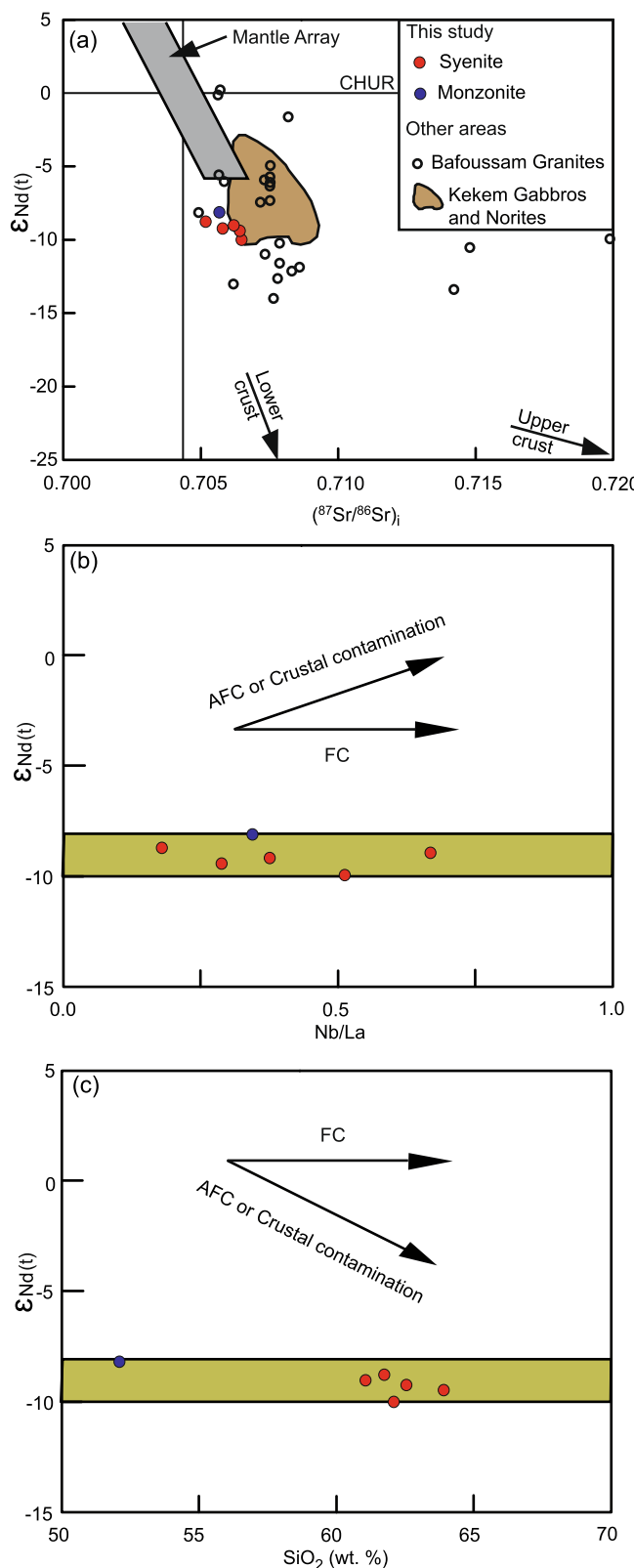


Fig. 10. (a) Plot of Epsilon Nd(t) vs. $(^{87}\text{Sr}/^{86}\text{Sr})_i$ from this study and published data of shoshonitic granites from Bafoussam (Djouka-Fonkwe et al., 2008) and shoshonitic gabbros and norites from Kekem (Kwékam et al., 2013), both in western Cameroon. Also plotted are trends to Lower and Upper Crust (after Jahn et al., 1999). CHUR (chondritic uniform reservoir). Plot of (b) Nb/La ratio and (c) silica (wt.%) vs. Epsilon Nd(t), indicating fractional crystallization.

(Al₂O₃, Na₂O and K₂O) correlations of SiO₂ content (Fig. 8). Inverse correlation of silica with MgO and Fe₂O₃ (Fig. 8c, h) in these rocks indicates an early crystallization of ferro-magnesian minerals, while depletion in V (Fig. 8j) (along with Fe₂O₃ (Fig. 8h)) seems consistent with magnetite crystallization. Decrease in CaO (Fig. 8d) can be attributed to possible clinopyroxene fractionation as early removal of plagioclase is ruled out by the non-linear relationship between SiO₂ and Al₂O₃ (Fig. 8b). Plagioclase and K-feldspar may coexist in the most evolved rocks, as testified by high Al₂O₃ and increasing alkali contents (Fig. 8e, f). The decrease in P₂O₅ (Fig. 8g) and Y (Fig. 8i) can be related to the fractionation of apatite while a decrease in TiO₂ (Fig. 8a) can be associated with the fractionation of titanite.

The presence of inherited zircon grains in samples YB21 and Y18 likely points to limited assimilation of an older crustal-derived material during crystallization and/or emplacement, which obviously had little effect on Sr and Nd isotope characteristics. All the above-mentioned geochemical parameters point towards fractional crystallization as the dominant process of magma evolution of the Linde syenitic massif.

6.4. Magma sources and melting-crystallization conditions

The geochemical consistency exhibited by the rocks of Linde massif (Fig. 8) suggests sources substantiated by the similarities in REE and trace element patterns (Fig. 9) and in Sr-Nd isotopes characteristics (Fig. 10a).

The trace element patterns of the studied rocks show a general similarity with average crust and LILE enrichment as compared to the lower continental crust. Some critical trace element ratios, such as Nb/U (6.8), Ta/U (0.4), Ce/Pb (2.6), Th/La (0.4) and Th/U (5.8) show a close similarity with the bulk continental crust (Nb/U = 6.2, Ta/U = 0.5, Ce/Pb = 3.9, Th/La = 0.3, Th/U = 4.3; Rudnick and Gao, 2003), further suggesting a predominantly crustal source for the Linde rocks.

Except for an anomalous mantle-like $\delta^{18}\text{O}_{\text{zn}}$ value of 5.3‰ recorded in the sample Y18 (Fig. 12a), the overall $\delta^{18}\text{O}_{\text{zn}}$ values of Neoproterozoic zircon grains (5.7–7.6‰; n = 46 of 47) from samples Y18, YB8, YB15 and YB21 are within the range for continental igneous zircon. These $\delta^{18}\text{O}_{\text{zn}}$ values reflect feature from the sources as the possibility of their evolution being related to fractional crystallization is ruled out by the lack of any covariance between $\delta^{18}\text{O}_{\text{zn}}$ and SiO₂ (Fig. 12b).

The zircon $\epsilon_{\text{Hf}}(t)$ isotopic compositions of 600 Ma (YB8 and YB15) rocks vary from -14.7 to -10.9 (Fig. 12c), suggesting a significant crustal component of model age ($T_{\text{DM2}} = 2209\text{--}2441$ Ma (Fig. 12d)). In the works of Ayonta Kenne et al. (2021), the position of zircon grains from the Linde granitoids within the fields of continental zircons in the U/Yb versus Hf and Y discrimination diagrams between continental and oceanic crust zircons (Grimes et al., 2007), and within the field of the arc-magmatic array in the U/Yb versus Nb/Yb discrimination diagram between the mantle-zircon array and the arc-magmatic array (Grimes et al., 2015), also suggest the crustal source. On the other hand, the 630 and 660 Ma (Y18 and YB21) zircon grains have $\epsilon_{\text{Hf}}(t)$ values ranging from -11.5 to +3.2 and from +0.0 to +3.0, respectively (Fig. 12c, d), underlining a mantle-derived component in the predominantly crustal source (T_{DM2} range 1345–2084 Ma). The presence of occasional mafic enclaves in sample YB21 support the presence of a mantle-derived component in the rock source. Thus, considering the features discussed above, at least two sources geochemically close but with different $^{176}\text{Hf}/^{177}\text{Hf}$ zircon isotope characteristics were involved in the formation of the Linde massif. We envisage that a crustal source with a mantle component (towards west) produced the 660 and 630 Ma rocks (identical initial $^{176}\text{Hf}/^{177}\text{Hf}$ zircon isotopes of 0.282368–0.282453 and 0.282061–0.282476); a crustal source (toward east) with less or negligible mantle input produced the ca. 600 Ma rocks (initial $^{176}\text{Hf}/^{177}\text{Hf}$ zircon isotopes of 0.281992–0.282097). The 2000 Ma inherited zircon grains in Y18 and YB21, have $\epsilon_{\text{Hf}}(t)$ ranging from -16.6 to -2.6 with the T_{DM2} ages at 2766–3548 Ma, suggesting melting of the reworked crustal material segregated at Archean times.

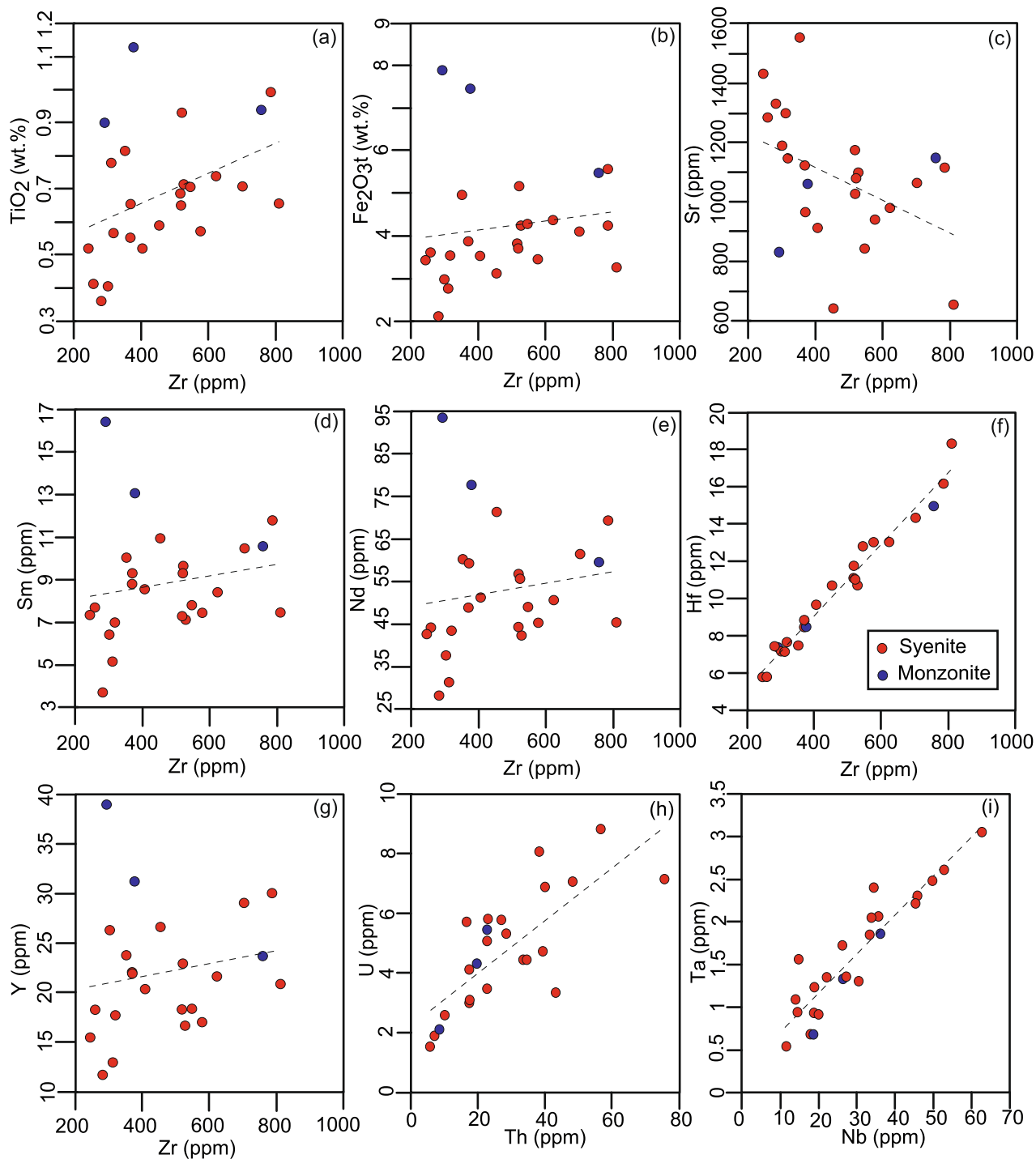


Fig. 11. (a-g) Selected major (wt.%) and trace elements (ppm) vs. Zr (ppm) for the rocks from the Linte massif to evaluate post-crystallization mobility of elements. Correlation trend is shown by a dashed line. (h) U (ppm) vs. Th (ppm) and (i) Ta (ppm) vs. Nb (ppm) diagrams for the rocks from the Linte massif showing sub-linear correlations, suggesting geochemical similarity of sources.

The positive $\epsilon_{\text{Hf}}(t)$ values (of some Neoproterozoic zircon grains) coupled with negative whole rocks $\epsilon_{\text{Nd}}(t)$ values in samples Y18 and YB21 suggest a decoupling of Hf-Nd isotopic signatures, which could either be the effect of inheritance from the magma source or a result of disequilibrium melting (e.g., Yu et al., 2017). Zircon grains do not dissolve completely during the disequilibrium melting, therefore, they could retain a significant fraction of ^{177}Hf from the parent rocks (Tang et al., 2014), thus elevating the $^{176}\text{Hf}/^{177}\text{Hf}$ ratios of the melt and consequent decoupling from the $^{143}\text{Nd}/^{144}\text{Nd}$ ratios (Zhang et al., 2019). The analyzed rocks have 245 to 810 ppm Zr, which is significantly

higher than the crustal abundance (100–200 ppm; Taylor and McLennan, 1985). These rocks display Hf and Zr positive anomalies in the primitive mantle-normalized diagrams (Fig. 9b) and their low Lu/Hf ratios (0.02–0.06), suggest that zircon might have been significantly accumulated in the magma source through (almost) complete dissolution (therefore in equilibrium) rather than removed (e.g., Zhang et al., 2019), thus ruling out the possibility of disequilibrium melting. Therefore, the decoupled Nd-Hf isotopic features observed in the 630 and 660 Ma samples can be interpreted as the inherited features from the (predominantly crustal) magma source.

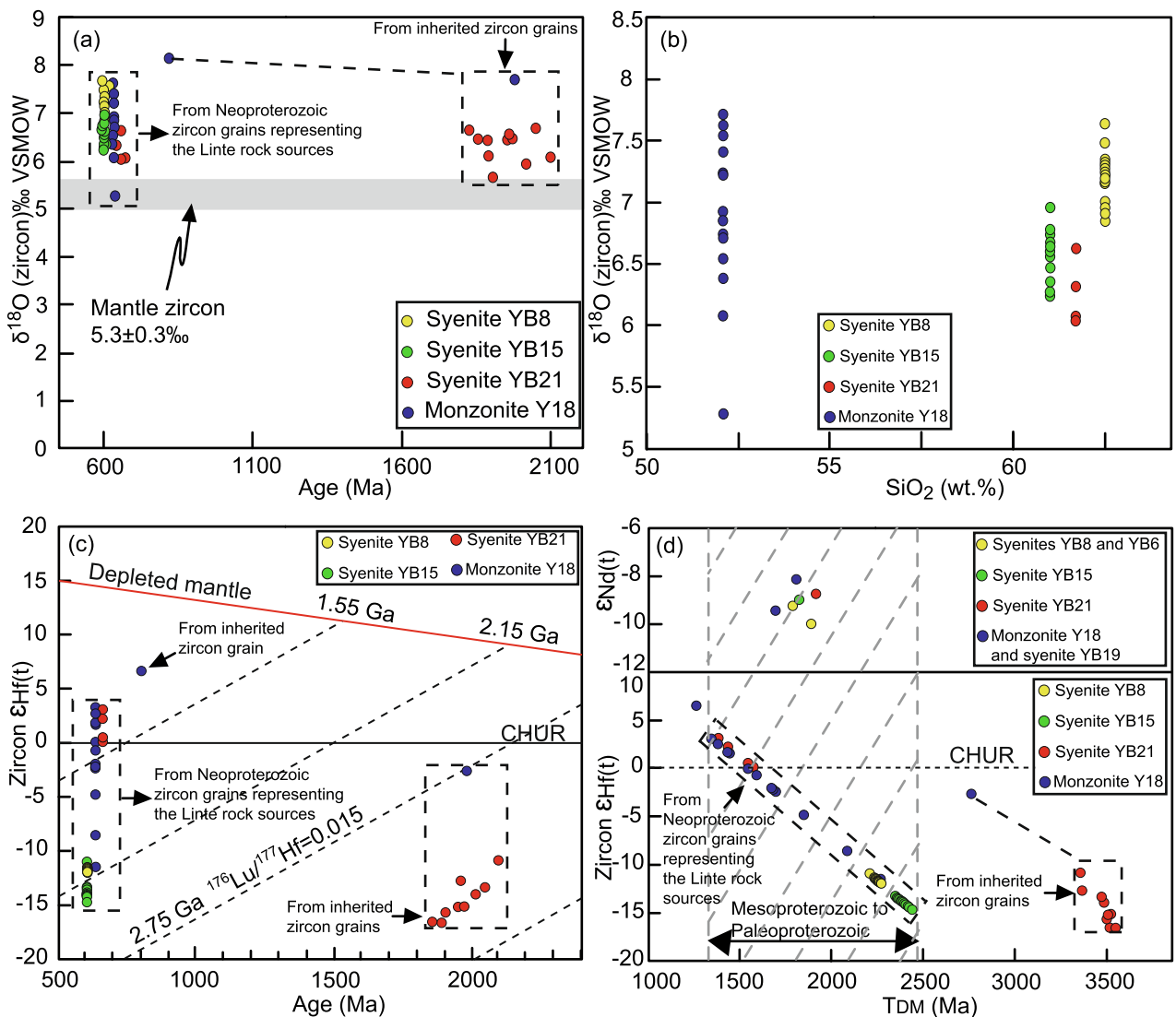


Fig. 12. (a) Plot of Epsilon $\text{Hf}(t)$ vs. U-Pb zircon age for the rocks from the Linte massif ($^{176}\text{Lu}/^{177}\text{Hf} = 0.015$, Griffin et al., 2002, 2004). (b) Values of $\delta^{18}\text{O}$ (zircon) vs. individual U-Pb zircon age of corresponding rocks for the Linte massif. (c) Plot of $\delta^{18}\text{O}$ (zircon) vs. SiO_2 (wt %) for the rocks from the Linte massif. (d) Plot of Epsilon $\text{Hf}(t)$ and $\text{Nd}(t)$ vs. T_{DM} ages (T_{DM} for $\epsilon_{\text{Nd}}(t)$ and $T_{\text{DM}2}$ for $\epsilon_{\text{Hf}}(t)$).

6.5. Temperature-oxygen fugacity conditions

The TiO_2 - SiO_2 temperature estimates (Green and Pearson, 1986) suggest a < 900 °C near-liquidus temperatures for the Linte massif rocks (Fig. 8a) also supported by the apatite saturation thermometry estimates (Green and Watson, 1982) that cluster around 950 °C for most of the samples (Fig. 8g). Zircon chemistry has been a popular thermometer and oxygen fugacity gauge for magmatic rocks (Watson and Harrison, 1983; 2005; Ballard et al., 2002; Miller et al., 2003; Smythe and Brenan, 2016; Chang et al., 2020; Lu et al., 2021; Wang et al., 2022). Watson and Harrison (1983) proposed a geothermometer for the estimation of zircon saturation temperatures (T_{Zr}) of primary magma, through the empirical equation: $T_{\text{Zr}} = 12900/[2.75 + 0.85 \text{M} + \ln(496000/\text{Zr}_{\text{melt}})]$. Results for the Linte massif range from 735 to 967 °C (Table 5) with an average of 874 °C pointing toward hot granitoids ($T_{\text{Zr}} > 800$ °C; Miller et al., 2003). The Ti-in-zircon is an important thermometer in estimating thermal conditions of magma and crystallization temperature (Watson and Harrison, 2005; Sepidbar et al., 2018; Chang et al., 2020 and references therein). The Ti-in-zircon temperatures (calculated using the software Geo-fO₂; Li et al., 2019) of 660, 630 and 600 Ma Linte massif zircon grains (except the discordant ones) fall within 702–806 °C, 678–818 °C

(with an outlier at 2992 °C) and 827–1013 °C temperature range, respectively. The unrealistically high 2992 °C determined in an isolated case of sample Y18, is related to an anomalous Ti content (10448 ppm), either due to alteration in the source or some analytical error (Gudelius et al., 2020). The estimated average temperature for the 660 Ma (756 °C) and 630 Ma (747 °C, excluding the outlier) samples are similar and significantly lower than the 600 Ma (925 °C) samples. This temperature is consistent with the (853–927 °C) range, reported by Ayonta Kenne et al. (2021) for the Linte granitoids. The wide range of Ti-in-zircon temperatures from 678 °C to 1013 °C suggests partial melting in the deeper layers, probably within the lower continental crust of the CAFB. These inferences are also in agreement with Ayonta Kenne et al. (2021) who estimated a Ti-in-zircon temperatures range of 574–1137 °C.

The calculated $\text{Ce}^{4+}/\text{Ce}^{3+}$ ratio (through Geo-fO₂, using the model of Ballard et al., 2002) in the Neoproterozoic zircon grains (Supplementary material 4) varies from 14.8 to 126.6, 5.5 to 323.3, and 6.9 to 124.1, for ca. 660, 630 and 600 Ma samples, respectively. Such $\text{Ce}^{4+}/\text{Ce}^{3+}$ ratios indicate a change in the magmatic oxidation state and fO₂ in these samples (e.g., Ballard et al., 2002; Trail et al., 2011). The estimated fO₂ (calculated through Geo-fO₂, using the oxybarometer of Trail et al. (2011)) presented in Supplementary material 4, ranges from –20.0 to

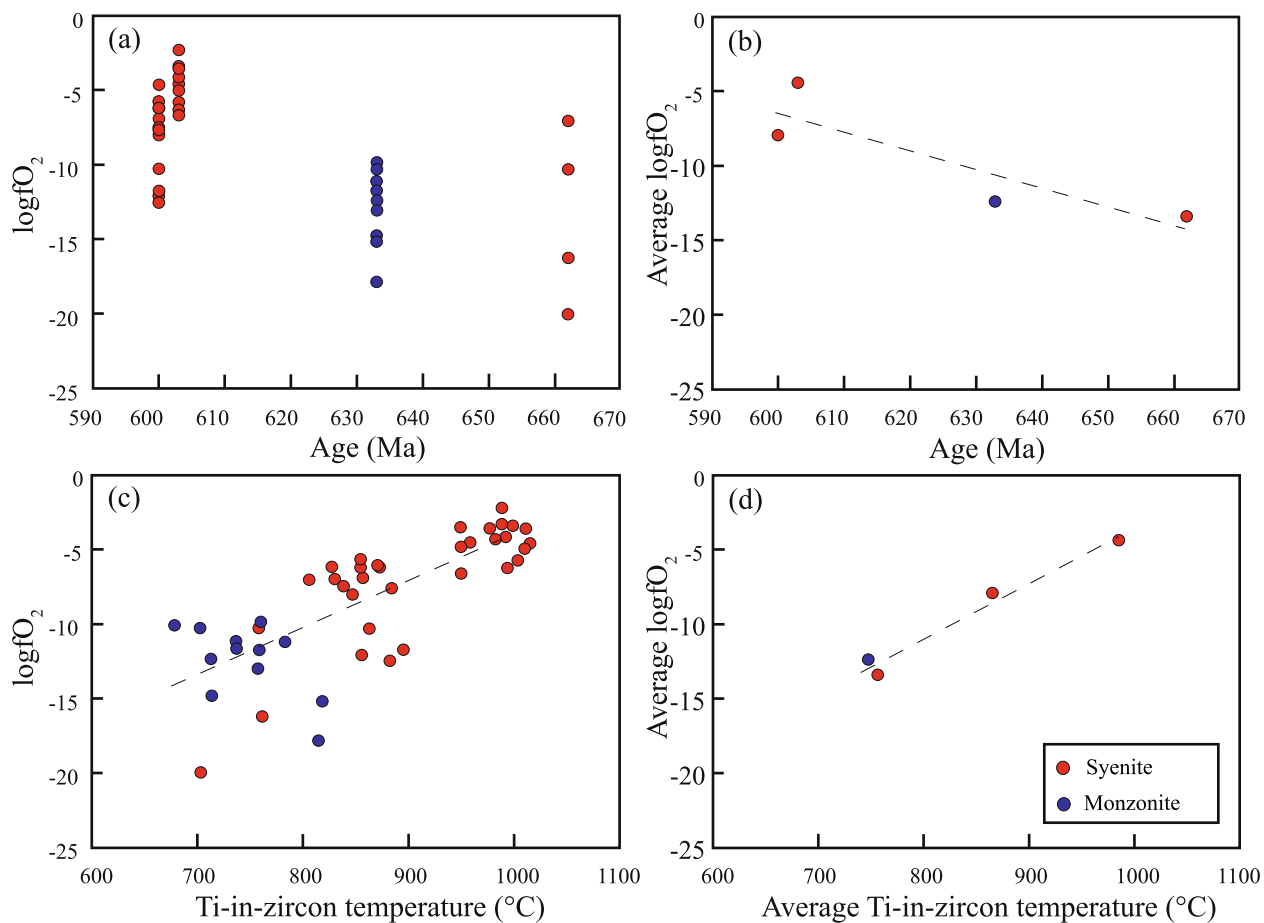


Fig. 13. (a) $\log fO_2$ and (b) average $\log fO_2$ vs. crystallization age of zircons from rocks of the Linte massif. (c) $\log fO_2$ and (d) average $\log fO_2$ vs. Ti-in-zircon temperature for the rocks from the Linte massif.

-7.0, -17.8 to -9.9 (outlier at 15.0) and -12.5 to -2.3 from old to young rock, respectively. The averages for the ca. 660 Ma (-13.4) and 630 Ma (-12.4 excluding the outlier 15.0) samples define a close cluster and are significantly lower than the average for the ca. 600 Ma samples (ca. -6.2). Therefore, the $\log fO_2$ of zircon grains decreases from the youngest ca. 600 Ma samples (containing a prevalent crustal component) to the oldest, ca. 660 Ma through 630 Ma samples (containing crustal component with a minor mantle input) (Fig. 13a, b) and/or increases with increasing Ti-in-zircon temperatures (Fig. 13c, d), indicating the heterogeneous fO_2 of the magma sources.

6.6. Tectonic implications

The Pan-African magmatism in the CAFB can be resolved into pre-, syn- and late-tectonic plutonism at ca. 660–580 Ma (e.g., Toteu et al., 1987, 2001; Kwékam et al., 2010; Dawai et al., 2013) and post-tectonic events at ca. 580–560 Ma (e.g., Kwékam et al., 2013; Li et al., 2017). In the Zr vs. (Nb/Zr)_N tectonic discriminant diagram of Thiéblemont and Tegrey (1994) (Fig. 14a) and Yb vs. Ta diagram of Pearce (1984) (Fig. 14b) the samples plot in collision (continent–continent collision) and volcanic arc granite (VAG) fields (Fig. 14a, b). Their shoshonitic nature, high Al₂O₃ and low TiO₂ contents also indicate an arc-setting (Müller et al., 1993). The presence of both continent–continent collision and arc-related features in the Linte massif suggests an active continental margin region. The subduction signature in the magma source is supported by the Nb-Ta depletion (e.g., Pearce, 1982; Kay and Mahlburg-Kay, 1991). Therefore, we can assume that lithospheric mantle-derived magma before major collision acted as heat source that triggered partial melting in the basement rocks (sources) of the Linte

massif (Fig. 15).

The arguments presented above lead to the inference that the Linte massif was emplaced during 660 and 600 Ma, concomitant with the Pan-African peak deformation. The emplacement at ca. 660 Ma can be attributed to early stages of subduction which developed in continent–continent collision. The presence of 650–600 Ma (Ar/Ar-Amphibole) MORB like signatures in amphibolites from the Yaounde Group corroborates the existence of a Neoproterozoic oceanic crust in the CAFB to the north of Congo Craton (Owona et al., 2013). Initial $^{176}\text{Hf}/^{177}\text{Hf}$ zircon isotope ratios in the range between 0.282368 and 0.282453, and $\epsilon\text{Hf(t)}$ values ranging from +0.0 to +3.0 (Fig. 12c, d), indicate some mantle component in the crustal melts. We can assume that the mantle component was partially melted during the subduction of Yaounde oceanic crust that mingled with crustal/basement rocks, leading to such isotopic compositions (Fig. 15). This inference is further supported by the shoshonitic affinity and subduction-related geochemical features, such as low Nb and Ta (e.g., YB21, Nb = 11.6 and Ta = 0.6). At the time of the 633 Ma measured age, the magma source did not substantially change (crustal materials mingled with mantle components) since the Neoproterozoic zircon grains from the representative sample Y18 show initial $^{176}\text{Hf}/^{177}\text{Hf}$ values of 0.282061–0.282476, and some $\epsilon\text{Hf(t)}$ values (the positive ones) form +0.1 to +3.2 close to the ones from YB21 (Fig. 12c, d). We can assume that the early subduction setting developed in continent–continent collision, resulting in regional scale crustal thickening (ca. 630–620 Ma; Ngako et al., 2008). The youngest age we measured, at 600 Ma, is characterized by crustal derived melts, as shown in their initial $^{176}\text{Hf}/^{177}\text{Hf}$ zircon isotope ratios (0.281992–0.282097) and $\epsilon\text{Hf(t)}$ values (-14.7 to -10.9) in crustal range (Fig. 12c, d). The 600 Ma age is within the 613–585 Ma age

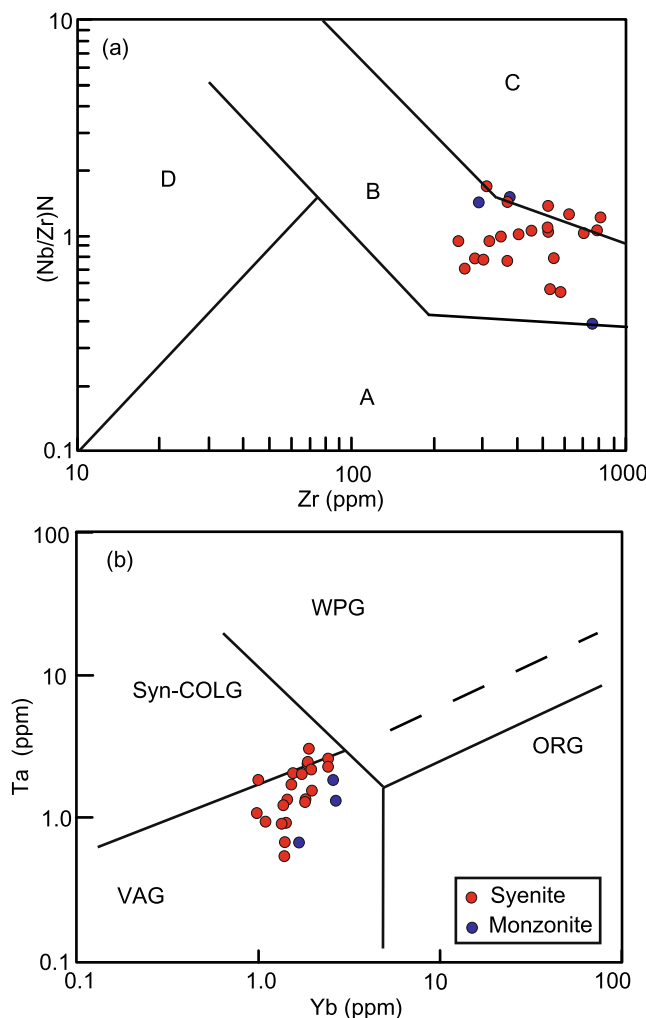


Fig. 14. Plots for geochemical tectonic discriminant diagrams for the Linte massif rocks. (a) Zr (ppm) vs. $(\text{Nb}/\text{Zr})_N$ (after Thiéblemont and Tegyey, 1994). (b) Yb (ppm) versus Ta (ppm) (after Pearce et al., 1984). A (subduction zone), B (continent–continent collision zone), C (alkaline intraplate zone), D (peraluminous continent–continent collision zone), VAG (Volcanic arc granite), WPG (Within plate granite), Syn-COLG (Syn-collision granite), ORG (Ocean ridge granite).

bracket correspondent to left lateral wrench movements in Cameroon (Ngako et al., 2008). Our findings are consistent with the two proposed models of the evolution of the CAFB, since rocks show subduction-related features, and continent–continent collision and arc-related features (suggesting an active continental margin). Geophysical data shown that the thickness of the crust is more elevated beneath the Congo craton than beneath terranes situated toward north (e.g., Adamawa-Yade and northern domains) (Goussi Ngalamo et al., 2017, 2018). The presence of a denser lower crust under the southern part of the Adamawa-Yade domain can be attributed to the densification of an under-thrust portion of the Congo craton (Goussi Ngalamo et al., 2017), which can be the tail of the northward subducted Yaounde oceanic crust (Tchakounté et al., 2021). Therefore the rocks of the Linte syenitic massif could be associated with northward subduction (e.g., Toteu et al., 2006a; Gentry et al., 2021; Tchakounté et al., 2021).

The 660–600 Ma magmatism in the CAFB of the Linte region was sourced from a largely crustal (Mesoproterozoic to Paleoproterozoic) protoliths with a minor mantle input (Fig. 12c, d). During the early stages of subduction (before continent–continent collision) and crustal thickening, some mantle component possibly mingled with the shallower crustal materials to yield moderately high $\delta^{18}\text{O}$ values. The lower

crustal rocks partial melted during the left lateral wrench movements in Cameroon (613–585 Ma; Ngako et al., 2008).

The study rocks show *syn-tectonic* ages while their geochemical compositions point to shoshonitic feature which is typical to post-tectonic setting. This suggests that the rocks could be *syn-* to *post-tectonic*. The calc-alkaline feature, which is the typical magma series of subduction-related magmatism could have been totally evolved to shoshonitic feature during the *syn-* to *post-tectonic* transition processes in the final stages of orogeny (e.g., Liégeois et al., 1998) which, unfortunately have no age (*post-tectonic*) recorded in the study rocks. Therefore, the geochemical characteristic (shoshonitic) of the Linte syenitic massif points to the composition of sources and not to its geotectonic setting (e.g., Pearce et al., 1984; Sylvester, 1989).

Pan-African plutons with shoshonitic affinity are known from the western part of Cameroon, such as at Bangangte (syenomonzonite dated at 585 ± 4 Ma and 583 ± 4 Ma; Tchouankoue et al., 2016) and Kekem (gabbros dated at 576 ± 4 Ma; Kwékam et al., 2013). The shoshonitic rocks are also enclosed in plutonic complexes in Bafoussam (biotite granitoid, Djouka-Fonkwe et al., 2008) and Bayon (gabbros, Ngo Belnou et al., 2013). The Bangangte syenomonzonites were generated by partial melting of an enriched mantle source metasomatized through previous subduction process(es), and most likely emplaced within a post-collisional setting (Tchouankoue et al., 2016). The Kekem gabbroic rocks were derived from a subduction-modified mantle source (metasomatized lithospheric mantle) contaminated by the Paleoproterozoic crustal rocks and emplaced in a post-collisional setup (Kwékam et al., 2013). The Bafoussam biotite granitoids are metaluminous to weakly peraluminous and are classified as highly fractionated I-type granitoids. They show volcanic arc to subduction and collisional tectonic features and were derived from a variable metasomatized primitive source. Their ages are estimated from the neighboring high-K calc-alkaline two-mica granitoids dated between 558 ± 8 Ma and 564 ± 7 Ma (Djouka-Fonkwe et al., 2008). The Bayon rocks show I-type granite and metaluminous characters, and occur along with gabbro. They were generated by partial melting of subcontinental lithospheric mantle (Mesoproterozoic), and were emplaced between 547 ± 26 Ma and 580 ± 13 Ma in a subduction to collision tectonic environment (Ngo Belnou et al., 2013). In the Pernambuco-Alagoas (PEAL domain in northeast Brazil), shoshonitic magmatism is represented by the Aguas Belas (syenogranite dated at 588 ± 4 Ma; Silva Filho et al., 2010, 2013) and the Guarany (granite and diorite dated at 573 ± 4 Ma; Ferreira et al., 2015). The occurrence of shoshonitic plutons in these regions of Africa and South America also provide clues for geographical proximity of northeast Brazil and central Africa, prior to the opening of the South Atlantic Ocean (Brito Neves et al., 2002; Van Schmus et al., 2008; Nardi et al., 2021). The ca. 630–600 Ma time interval representing a collisional phase (crystallizations) in the Linte massif is also consistent with the 630 and 600 Ma main convergence of the Brasiliano Orogeny in the Borborema Province (Neves et al., 2008, 2009; Van Schmus et al. 2008). A change from extensional to contractional tectonic setting occurred at ca. 640–630 Ma, and from collision to lateral movements at ca. 590–580 Ma in the Transversal Domain of the Borborema Province that seem to correspond with the tectonic model of the study area emplaced at ca. 660–600 Ma.

7. Conclusion

The significant findings of the study are listed below.

- (1) The Linte syenitic pluton represents a peak of magmatism during 660–600 Ma (lasting at least 60 Ma), *syn-collisional* with the Pan-African orogeny in the Central Africa Fold Belt.
- (2) The massif is mildly alkaline, shoshonitic and exhibits I-type granite geochemical characteristics. It was likely formed from two different sources geochemically close but likely characterized by different magma components, as zircon eHf(t) isotopic compositions vary from -11.5 to $+3.2$ and from -14.7 to -10.9 .

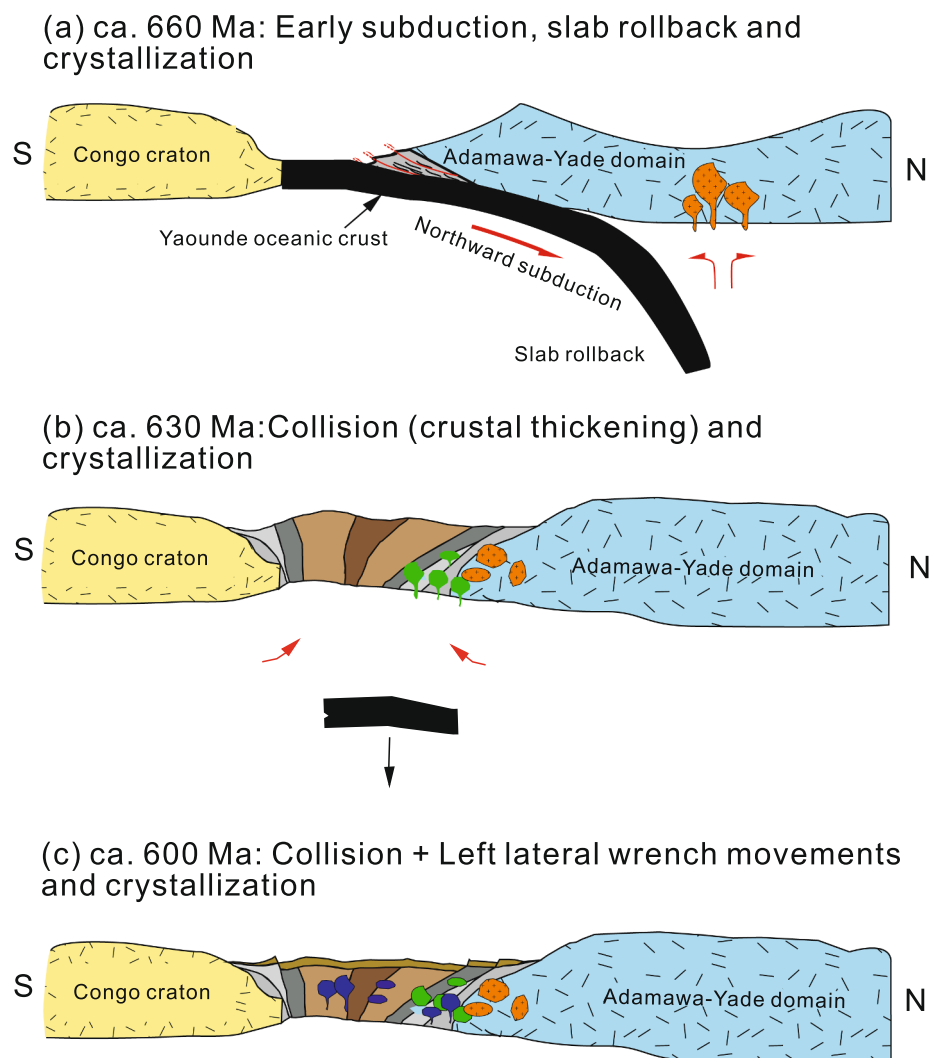


Fig. 15. Schematic representation of the geodynamic evolution of the Linte syenitic massif during early subduction (ca. 660 Ma), crustal thickening (ca. 630 Ma) and left lateral wrench movements (ca. 600 Ma).

The magmas were emplaced *syn-tectonically* during early subduction and followed by collision during the period 660–600 Ma. Fractional crystallization seems to be the main process which acted during magmas evolution.

- (3) The Linte massif shows Paleoproterozoic Nd-T_{DM} model ages at ca. 1700–1900 Ma and a large range of the zircon Hf-T_{DM2} at ca. 1300–2400 Ma. These model ages combined with the εNd(t) and zircon εHf(t) values of −10.0 to −8.1 and −14.7 to +3.2, respectively, indicate the contribution of Mesoproterozoic to Paleoproterozoic reworked crustal and mantle materials in the sources.

CRediT authorship contribution statement

Bovari Syprien Yomeun: Conceptualization, Investigation, Writing – original draft, Writing – review & editing. **Wei Wang:** Conceptualization, Investigation, Writing – original draft, Writing – review & editing. **Michele Sandra Kamguia Kamani:** Writing – review & editing. **Jean Pierre Tchouankoue:** Writing – review & editing. **Ying-De Jiang:** Investigation, Data curation, Writing – review & editing. **Si-Fang Huang:** Investigation, Data curation, Writing – review & editing. **Kevin Igor Azeuda Ndonfack:** Writing – review & editing. **Er-Kun Xue:** Writing – review & editing. **Gui-Mei Lu:** Investigation, Data curation, Writing – review & editing. **Emmanuel Archelaus Afanga Basua:**

Writing – review & editing.

Declaration of Competing Interest

The authors declare that they have no known competing financial interests or personal relationships that could have appeared to influence the work reported in this paper.

Acknowledgements

This study is part of the ongoing PhD thesis of the first author, at the School of Earth Sciences, China University of Geosciences, Wuhan. It was supported by the National Natural Science Foundation of China (NSFC 41972242), the MOST Special Fund from the State Key Laboratory of Geological Processes and Mineral Resources (MSFGPMR 01-1) and research grant of State Key Laboratory of Isotope Geochemistry (SKLabIG-KF-18-07), Guangzhou Institute of Geochemistry, Chinese Academy of Sciences. We thank Zhaochu Hu for help with (MC)-LA-ICPMS analyses, Abing Lin for the whole-rock geochemical analyses, Cai Xinglan and Li Sun for laboratory assistance, Dr. Lucas Mouafou and Just-Christ Yimgang for their supports and advices. Professor Manoj Pandit is greatly thanked for language polishing. The China Scholarship Council (CSC) is deeply appreciated for granting scholarship (2017GXZ015788) to the first author. We thank Professor Armin Zeh and two anonymous

reviewers for their constructive comments on different versions that have helped in improving the presentation and interpretation. We also like to thank Kamal Ali for additional comments and editorial efforts.

Appendix A. Supplementary material

Supplementary data to this article can be found online at <https://doi.org/10.1016/j.precamres.2022.106675>.

References

- Abdelsalam, M.G., Liégeois, J.-P., Stern, R.J., 2002. The Saharan Metacraton. *J. Afr. Earth Sc.* 34 (3-4), 119–136.
- Almeida, F.F., Hasui, Y., Brito De Neves, B.B., Fuck, R.A., 1981. Brazilian structural provinces. *Earth Sci. Rev.* 17, 1–29.
- Ayonta Kenne, P., Tanko Njiosseu, E.L., Ganno, S., Ngnotue, T., Fossi, D.H., Hamdja Ngonfiri, A., Nga Essomba, P., Nzenti, J.P., 2021. Zircon trace element geochemistry and Ti in-zircon thermometry of the Linté Pan-African granitoids, Central Cameroon: Constraints on the genesis of host magma and tectonic implications. *Geol. J.* 1–19 <https://doi.org/10.1002/gj.4208>.
- Ballard, J.R., Palin, M.J., Campbell, I.H., 2002. Relative oxidation states of magmas inferred from Ce(IV)/Ce(III) in zircon: Application to porphyry copper deposits of northern Chile. *Contrib. Miner. Petrol.* 144 (3), 347–364.
- Belousova, E., Griffin, W., O'Reilly, S.Y., Fisher, N., 2002. Igneous zircon: trace element composition as an indicator of source rock type. *Contrib. Miner. Petrol.* 143 (5), 602–622.
- Berger, J., Caby, R., Liégeois, J.-P., Mercier, J.-C., Demaiffe, D., 2011. Deep inside a neoproterozoic intra-oceanic arc: growth, differentiation and exhumation of the Amalaouala complex (Gourma, Mali). *Contrib. Miner. Petrol.* 162 (4), 773–796.
- Bouvier, A., Vervoort, J.D., Patchett, P.J., 2008. The Lu-Hf and Sm-Nd isotopic composition of CHUR: Constraints from unequilibrated chondrites and implications for the bulk composition of terrestrial planets. *Earth Planet. Sci. Lett.* 273 (1-2), 48–57.
- Bouyou Houketchang, M., Toteu, S.F., Deloule, E., Penaye, J., Van Schmus, W.R., 2009. U-Pb and Sm-Nd dating of high-pressure granulites from Tcholliré and Banyo regions: evidence for a Pan-African granulite facies metamorphism in north-central Cameroon. *J. Afr. Earth Sc.* 54 (5), 144–154.
- Bley de Brito Neves, B., Van Schmus, W.R., Fetter, A., 2002. North-western Africa-Northeastern Brazil: major tectonic links and correlation problems. *J. Afr. Earth Sc.* 34 (3-4), 275–278.
- Caby, R., 2003. Terrane assembly and geodynamic evolution of central-western Hoggar: a synthesis. *J. Afr. Earth Sc.* 37 (3-4), 133–159.
- Castaing, C., Feybesse, J.L., Thiéblemont, D., Triboulet, C., Chévremont, P., 1994. Paleogeographical reconstructions of the Pan-African/Brasiliano orogen: closure of an oceanic domain or intracontinental convergence between major blocks? *Precambr. Res.* 69, 327–344.
- Chang, Z.-G., Dong, G.-C., Somarin, A.K., 2020. U-Pb Dating and Trace Element Composition of Zircons from the Gujiao Ore-Bearing Intrusion, Shanxi, China: Implications for Timing and Mineralization of the Guojialiang Iron Skarn Deposit. *Minerals* 10 (316), 1–14.
- Chappell, B.W., White, A.J.R., 1992. I- and S-type granites in the Lachlan Fold Belt. *Trans. Roy. Soc. Edinburgh: Earth Sci.* 83, 1–26.
- Chebeu, C., Ngo Nlend, C.D., Nzenti, J.P., Ganno, S., 2011. Neoproterozoic High-K Calc-Alkaline Granitoids from Bapa-Batié, North Equatorial Fold Belt, Central Cameroon: Petrogenesis and Geodynamic Significance. *Open Geol. J.* 5, 1–20.
- Corfu, F., Hanchar, J.M., Hoskin, P.W.O., Kinny, P.D., 2003. Atlas of zircon textures. *Rev. Mineral. Geochem.* 53, 469–500.
- Dawaï, D., Bouchez, J.L., Paquette, J.L., Tchameni, R., 2013. The Pan-African quartz-syenite of Guider (North-Cameroun): Magnetic fabric and U-Pb dating of a late-orogenic emplacement. *Precambr. Res.* 236, 132–144.
- Djouka-Fonkwé, M.L., Schulz, B., Schüssler, U., Tchouankoué, J.-P., Nzolang, C., 2008. Geochemistry of the Bafoussam Pan-African I- and S-type granitoids in western Cameroon. *J. Afr. Earth Sc.* 50 (2-4), 148–167.
- Ferreira, V.P., Sial, A.N., Pimentel, M.M., Armstrong, R., Guimarães, I.P., da Silva Filho, A.F., Lima, M.M.C., da Silva, T.R., 2015. Reworked old crust-derived shoshonitic magma: The Guarany pluton, Northeastern Brazil. *Lithos* 232, 150–161.
- Frost, B.R., Barnes, C.G., Collins, W.J., Arculus, R.J., Ellis, D.J., Frost, C.D., 2001. A geochemical classification for granitic rocks. *J. Petrol.* 42, 2033–2048.
- Ganwa, A.A., 2005. Les granitoïdes de Méiganga: Étude pétrographique, géochimique, structurale et géochronologique. Leur place dans la chaîne panafriacaine. Thèse de doctorat d'Etat, Université Yaoundé I, 162p.
- Ganwa, A.A., Frisch, W., Siebel, W., Ekodeck, G.E., Shang, C.K., Ngako, V., 2008. Archean inheritance in the pyroxene-amphibole-bearing gneiss of the Méiganga area (Central North Cameroon): Geochemical and $^{207}\text{Pb}/^{206}\text{Pb}$ age imprints. *Comptes Rendus Geosci.* 340 (4), 211–222.
- Ganwa, A.A., Klötzli, U.S., Digum Kepnamou, A., Hauzenberger, C., Horváth, P., 2018. Multiple Ediacaran tectonometamorphic events in the Adamawa-Yadé Domain of the Central Africa Fold Belt: Insight from the zircon U-Pb LAM-ICP-MS geochronology of the metadiorite of Meiganga (Central Cameroon). *Geol. J.* 53 (6), 2955–2968.
- Ganwa, A.A., Klötzli, U.S., Hauzenberger, C., 2016. Evidence for Archean inheritance in the pre-Pan-african crust of Central Cameroon: Insight from zircon internal structure and LA-MC-ICP-MS U-Pb ages. *J. Afr. Earth Sc.* 120, 12–22.
- Ganwa, A.A., Siebel, W., Frisch, W., Shang, C.K., 2011. Geochemistry of magmatic rocks and time constraints on deformational phases and shear zone slip in the Méiganga area, central Cameroon. *Int. Geol. Rev.* 33 (7), 759–784.
- Gentry, F.C., Nkoumbou, C., Numbem, J.T., Mukete, K.O., Tchouankoué, J.P., 2021. Petrology, geochemistry, Ar-Ar isotopes of an arc related calk-alkaline pluton from Mamb (Pan-African Yaoundé group, Cameroon): A testimony to the subduction of a hot oceanic crust. *Lithos* 384–385, 105973.
- Gerdes, A., Zeh, A., 2009. Zircon formation versus zircon alteration-new insights from combined U-Pb and Lu-Hf in-situ LA-ICP-MS analyses, and consequences for the interpretation of Archean zircon from the Limpopo Belt. *Chem. Geol.* 261, 230–243.
- Goussi Ngalamo, J.F., Bisso, D., Abdelsalam, M.G., Atekwanza, E.A., Katumwehe, A.B., Ekodeck, G.E., 2017. Geophysical imaging of metacratonisation in the northern edge of the Congo craton in Cameroon. *J. Afr. Earth Sc.* 129, 94–107.
- Goussi Ngalamo, J.F., Sobh, M., Bisso, D., Abdelsalam, M.G., Atekwanza, E., Ekodeck, G.E., 2018. Lithospheric structure beneath the Central Africa Orogenic Belt in Cameroon from the analysis of satellite gravity and passive seismic data. *Tectonophysics* 745, 326–337.
- Green, T.H., Pearson, N.J., 1986. Ti-rich accessory phase saturation in hydrous mafic-felsic compositions at high P-T. *Chem. Geol.* 54 (3-4), 185–201.
- Green, T.H., Watson, E.N., 1982. Crystallizations of apatite in natural magmas under high pressure, hydrous conditions, with particular reference to "ogenetic" rocks series. *Contrib. Miner. Petrol.* 79, 96–105.
- Griffin, W.L., Belousova, E.A., Shee, S.R., Pearson, N.J., O'Reilly, S.Y., 2004. Archean crustal evolution in the northern Yilarn Craton: U-Pb and Hf-isotope evidence from detrital zircons. *Precambr. Res.* 131, 231–282.
- Griffin, W.L., Pearson, N.J., Belousova, E., Jackson, S.E., van Achterbergh, E., O'Reilly, S.Y., Shee, S.R., 2000. The Hf isotope composition of cratonic mantle: LAM-MC-ICPMS analysis of zircon megacrysts in kimberlites. *Geochim. Cosmochim. Acta* 64 (1), 133–147.
- Griffin, W.L., Wang, X., Jackson, S.E., Pearson, N.J., O'Reilly, S.Y., Xu, X.S., Zhou, X.M., 2002. Zircon chemistry and magma genesis, SE China: in-situ analysis of Hf isotopes, Tonglu and Pingtan igneous complexes. *Lithos* 61, 237–269.
- Grimes, C.B., Wooden, J.L., Cheadle, M.J., John, B.E., 2015. 'Finger-printing' tectono-magmatic provenance using trace elements in igneous zircon. *Contrib. Miner. Petrol.* 170, 1–26.
- Grimes, C.B., John, B.E., Kelemen, P.B., Mazdab, F.K., Wooden, J.L., Cheadle, M.J., Hanghøj, K., Schwartz, J.J., 2007. Trace element chemistry of zircons from oceanic crust: A method for distinguishing detrital zircon provenance. *Geology* 35, 643–646.
- Gudelius, D., Zeh, A., Almeev, R.R., Wilson, A.H., Fischer, L.A., Schmitt, A.K., 2020. Zircon melt inclusions in mafic and felsic rocks of the Bushveld Complex-Constraints for zircon crystallization temperatures and partitioning coefficients. *Geochim. Cosmochim. Acta* 289, 158–181.
- Hu, Z., Liu, Y., Gao, S., Liu, W., Zhang, W., Tong, X., Lin, L., Zong, K., Li, M., Chen, H., Zhou, L., Yang, L., 2012. Improved in situ Hf isotope ratio analysis of zircon using newly designed X skimmer cone and jet sample cone in combination with the addition of nitrogen by laser ablation multiple collector ICP-MS. *J. Anal. At. Spectrom.* 27 (9), 1391.
- Jackson, S., Pearson, N., Griffin, W., Belousova, E., 2004. The application of laser ablation-inductively coupled plasma-mass spectrometry to in situ U-Pb zircon geochronology. *Chem. Geol.* 211 (1–2), 47–69.
- Jahn, B.-M., Wu, F., Lo, C.-H., Tsai, C.-H., 1999. Crust-mantle interaction induced by deep subduction of the continental crust: geochemical and Sr-Nd isotopic evidence from post-collisional mafic-ultramafic intrusions of the northern Dabie complex, central China. *Chem. Geol.* 157 (1–2), 119–146.
- Johnson, P.R., Andresen, A., Collins, A.S., Fowler, A.R., Fritz, H., Ghebreab, W., Kusky, T., Stern, R.J., 2011. Late Cryogenian-Ediacaran history of the Arabian-Nubian Shield: a review of depositional, plutonic, structural, and tectonic events in the closing stages of the northern East African Orogen. *J. Afr. Earth Sc.* 61 (3), 167–232.
- Kamguia Kamani, M.S., Wang, W., Tchouankoué, J.-P., Huang, S.-F., Yomeun, B., Xue, E.-K., Lu, G.-M., 2021. Neoproterozoic syn-collision magmatism in the Nkondjock region at the Northern border of the Congo Craton in Cameroon: Geodynamic implications for the Central African Orogenic belt. *Precambr. Res.* 353, 106015.
- Kanouo, N.S., Kouské, A.P., Lentz, D.R., Yongué, R.F., 2021. New Insights into Neoproterozoic-Cretaceous Events in the Mamfe Basin (SW Cameroon, Central Africa): Evidence from Textural Analyses, U-Th Composition, and U-Pb Zircon Geochronology from Granitic Basement. *J. Earth Sci.* 32 (6), 1472–1484.
- Kay, R.W., Mahlburg-Kay, S., 1991. Creation and destruction of lower continental crust. *Geol. Rundsch.* 80 (2), 259–278.
- Kröner, A., Stern, R.J., 2004. Pan-African Orogeny: Encyclopedia of Geology vol. 1, 1–12.
- Kusky, T.M., Abdelsalam, M., Tucker, R.D., Stern, R.J., 2003. Evolution of the East African and related orogens, and the assembly of Gondwana. *Precambr. Res.* 123 (2–4), 81–85.
- Kwékam, M., Affaton, P., Bruguier, O., Liégeois, J.-P., Hartmann, G., Njonfang, E., 2013. The Pan-African Kekem gabbro-norite (West-Cameroun), U-Pb zircon age, geochemistry and Sr-Nd isotopes: Geodynamical implication for the evolution of the Central African fold belt. *J. Afr. Earth Sc.* 84, 70–88.
- Kwékam, M., Dunkl, I., Foizing, E.M., Hartmann, G., Njanko, T., Tchoumekan, K.J., Njonfang, E., 2021. Syn-kinematic ferroan high-K I-type granites from Dschang in South-western Cameroon: U-Pb age, geochemistry and implications for crustal growth in the late Pan-African orogeny. *Geol. Soc., London, Special Publ.* 502 (1), 191–213.
- Kwékam, M., Liégeois, J.-P., Njonfang, E., Affaton, P., Hartmann, G., Tchoua, F., 2010. Nature, origin and significance of the Fomopéa Pan-African high-K calc-alkaline plutonic complex in the Central African Fold Belt (Cameroon). *J. Afr. Earth Sc.* 57 (1–2), 79–95.

- Kwékam, M., Talla, V., Fozing, E.M., Tcheumenak Kouémo, J., Dunkl, I., Njonfang, E., 2020. The Pan-African High-K I-Type Granites From Batié Complex, West Cameroon: Age, Origin, and Tectonic Implications. *Front. Earth Sci.* 8 (363), 1–14.
- Lerouge, C., Cocherie, A., Toteu, S.F., Milesi, J.P., Penaye, J., Tchameni, R., Nsifa, N.E., Fanning, C.M., 2006. SHRIMP U-Pb zircon dating for the Nyong Series, South West Cameroon. *J. Afr. Earth Sc.* 44, 413–427.
- Li, W., Cheng, Y., Yang, Z., 2019. Geo-fO2: Integrated software for analysis of magmatic oxygen fugacity. *Geochem. Geophys. Geosyst.* 20, 1–14.
- Li, X.H., Chen, Y., Tchouankoue, J.P., Liu, C.Z., Li, J., Ling, X.X., Tang, G.Q., Liu, Y., 2017. Improving geochronological framework of the Pan-African orogeny in Cameroon: New SIMS zircon and monazite U-Pb age constraints. *Precambr. Res.* 294, 307–321.
- Li, X.H., Long, W.G., Li, Q.L., Liu, Y., Zheng, Y.F., Yang, Y.H., Chamberlain, K.R., Wan, D. F., Guo, C.H., Wang, X.C., Tao, H., 2010. Penglai zircon megacrysts: A potential new working reference material for microbeam determination of Hf-O isotopes and U-Pb age. *Geostand. Geoanal. Res.* 34, 117–134.
- Li, X.H., Tang, G.Q., Gong, B., Yang, Y.H., Hou, K.J., Hu, Z.C., Li, Q.L., Liu, Y., Li, W.X., 2013. Qinghu zircon: A working reference for microbeam analysis of U-Pb age and Hf and O isotopes. *Geochimica* 58 (36), 4647–4654.
- Liégeois, J.-P., Abdelsalam, M.G., Ennih, N., Ouabadi, A., 2013. Metacraton: Nature, genesis and behavior. *Gondwana Res.* 23 (1), 220–237.
- Liégeois, J.-P., Navez, J., Hertogen, J., Black, R., 1998. Contrasting origin of post-collisional high-K calc-alkaline and shoshonitic versus alkaline and peralkaline granitoids. The use of sliding normalization. *Lithos* 45 (1–4), 1–28.
- Liew, T.C., Hofmann, A.W., 1988. Precambrian crustal components, plutonic associations, plate environment of the Hercynian Fold Belt central Europe: Indications from a Nd and Sr isotopic study. *Contrib. Miner. Petrol.* 98, 129–138.
- Liuy, Y.S., Gao, S., Hu, Z.C., Gao, C., Zong, K., Wang, D., 2010. Continental and Oceanic Crust Recycling-induced Melt-Peridotite Interactions in the Trans-North China Orogen: U-Pb Dating, Hf Isotopes and Trace Elements in Zircons from Mantle Xenoliths. *J. Petrol.* 51 (1–2), 537–571.
- Lu, G.-M., Wang, W., Tian, Y., Huang, S.-F., Xue, E.-K., Huang, B., 2021. Siderian mafic-intermediate magmatism in the SW Yangtze Block, South China: Implications for global 'tectono-magmatic lull' during the early Paleoproterozoic. *Lithos* 398–399, 106306.
- Ludwig, K.R., 2012. User's manual for Isoplot 3.75. A Geochronological Toolkit for Microsoft Excel. Berkeley Geochronol. Center Special Publ. 5, 1–75.
- Lugmair, G.W., Marti, K., 1978. Lunar initial $^{143}\text{Nd}/^{144}\text{Nd}$: differential evolution line of the lunar crust and mantle. *Earth Planet. Sci. Lett.* 39, 349–357.
- Maniar, P.D., Piccoli, P.M., 1989. Tectonic discrimination of granitoids. *Geol. Soc. Am. Bull.* 101, 635–643.
- McReath, I., Galindo, A.C., Dall'Agno, R., 2002. The Umarizal Igneous Association, Borborema Province, NE Brazil: Implications for the Genesis of A-Type Granites. *Gondwana Res.* 5 (2), 339–353.
- Middlemost, E.A.K., 1994. Naming materials in the magma/igneous rock system. *Earth-Sci. Rev.* 74, 193–227.
- Miller, C.F., McDowell, S.M., Mapes, R.W., 2003. Hot and cold granites? Implications of zircon saturation temperatures and preservation of inheritance. *Geology* 31, 529–532.
- Müller, D., Morris, B.J., Farrand, M.G., 1993. Potassic alkaline lamprophyres with affinities lamproites from the Karinya Syncline, South Australia. *Lithos* 30 (2), 123–137.
- Müller, D., Rock, N.M.S., Groves, D.I., 1992. Geochemical discrimination between shoshonitic and potassic volcanic rocks from different tectonic settings: a pilot study. *Mineral. Petrol.* 46, 259–289.
- Nardi, L.V.S., Bitencourt, M.d.F., Florisbal, L.M., Padilha, D.F., 2021. Shoshonitic Magmatic Series and the High Ba-Sr Granitoids: A Review with Emphasis on Examples from the Neoproterozoic Dom Feliciano Belt of Southern Brazil and Uruguay. *J. Earth Sci.* 32 (6), 1359–1373.
- Neves, S.P., 2003. Proterozoic history of the Borborema province (NE Brazil): Correlations with neighboring cratons and Pan-African belts and implications for the evolution of western Gondwana. *Tectonics* 22, 1031–1044.
- Neves, S.P., Bruguier, O., Bosch, D., Silva, J.M.R., Mariano, G., 2008. U-Pb ages of plutonic and metaplutonic rocks in southern Borborema Province (NE Brazil): Timing of Brasiliano deformation and metamorphism. *J. S. Am. Earth Sci.* 25, 285–297.
- Neves, S.P., Bruguier, O., da Silva, J.M.R., Bosch, D., Alcantara, V.C., Lima, C.M., 2009. The age distributions of detrital zircons in metasedimentary sequences in eastern Borborema Province (NE Brazil): Evidence for intracontinental sedimentation and orogenesis? *Precambr. Res.* 175 (1–4), 187–205.
- Ngako, V., Njonfang, E., 2008. Pan-African tectonics in northwestern Cameroon: Implication for the history of western Gondwana. *Gondwana Res.* 14 (3), 509–522.
- Ngako, V., Njonfang, E., 2011. Plates amalgamation and plate destruction, the Western Gondwana history. In: Closson, D. (Ed.), *Tectonics*. Intech Publisher, pp. 3–36.
- Ngo Belnoun, R.N., Tchouankoue, J.P., Itiga, I., Wambo, A.N.S., Owona, S., Koller, F., Thoni, M., 2013. Geochemistry of the Bayon plutonic complex-Western Cameroon. *Global J. Geol. Sci.* 11, 73–93.
- Njanko, T., Nédélec, A., Affaton, P., 2006. Synkinematic high-K calc-alkaline plutons associated with the Pan-African Central Cameroon shear zone (W-Tibati area): Petrology and geodynamic significance. *J. Afr. Earth Sc.* 44 (4–5), 494–510.
- Njiakak, G., Dör, W., Tchouankoue, J.P., Zulauf, G., 2008. U-Pb zircon and microfabrics data of (meta) granitoids of western Cameroon: Constraints on the timing of pluton emplacement and deformation in the Pan-African belt of Central Africa. *Lithos* 102, 460–477.
- Njiosseu, E.L.T., Nzenti, J.-P., Njanko, T., Kapajika, B., Nédélec, A., 2005. New U Pb zircon ages from Tonga (Cameroon): coexisting Eburrenean-Tansamazonian (2.1 Ga) and Pan-African (0.6 Ga) imprints. *Comptes Rendus Geosciences* 337 (6), 551–562.
- Nomo, N.E., Tchameni, R., Vanderhaeghe, O., Sun, F., Barbey, P., Tekoum, L., Fosso, P. M., Eglinger, A., Saha Fouotsa, N.A., 2017. Structure and LA-ICP-MS zircon U-Pb dating of syntectonic plutons emplaced in the Pan-African Banyo-Tcholliré shear zone (central north Cameroun). *J. Afr. Earth Sci.* 131, 251–271.
- Nzenti, J.P., Barbey, P., Macaudière, J., Soba, D., 1988. Origin and evolution of late Precambrian high-grade Yaounde gneisses. *Precambr. Res.* 38, 91–109.
- Nzenti, J.P., Minyem, D., Tchouankoue, J.P., Belinga, S.E., 2001. Le Panafricain. In *Histoire Géologique du Cameroun*. S.E. Belinga (Ed.), *Les Classiques Camerounais*, pp. 39–55.
- Owona, S., Mbola-Ndzana, S.P., Mpesse, J.E., Mvondo Ondo, J., Schulz, B., Pfander, J., Jegouzo, P., Affaton, P., Ratschbacher, L., Ekodeck, G.E., 2013. Petrogenesis of amphibolites from the Neoproterozoic Yaounde Group (Cameroun, Central Africa): evidence of MORB and implications on their geodynamic evolution. *Comunicações Geológicas* 100 (1), 5–13.
- Pearce, J.A., 1982. Trace element characteristics of lavas from destructive plate margins. In: Thorpe, R.S. (Ed.), *Andesites*. John Wiley, New York, pp. 525–548.
- Pearce, J.A., Harris, N.B.W., Tindale, A.G., 1984. Trace element discrimination diagrams for the tectonic interpretation of granitic rocks. *J. Petrol.* 25 (4), 956–983.
- Pearce, J.A., Peate, D.W., 1995. Tectonic Implications of the Composition of Volcanic ARC Magmas. *Annu. Rev. Earth Planet. Sci.* 23 (1), 251–285.
- Peccerillo, A., Taylor, S.R., 1976. Geochemistry of Eocene calc-alkaline volcanic rocks from the Kastamonu area, northern Turkey. *Contrib. Miner. Petrol.* 58 (1), 63–81.
- Penaye, J., Kröner, A., Toteu, S.F., Van Schmus, W.R., Doumnang, J.-C., 2006. Evolution of the Mayo Kebbi region as revealed by zircon dating: an early (ca. 740 Ma) Pan-African magmatic arc in south-western Chad. *J. Afr. Earth Sc.* 44 (4–5), 530–542.
- Penaye, J., Toteu, S.F., Michard, A., Bertrand, J.-M., Dautel, D., 1989. Reliques granulitiques d'âge Proterozoïque inférieur dans la zone mobile Panafricaine d'Afrique Centrale au Cameroun; Géochronologie U-Pb sur zircons. *Comptes Rendus Académiques de Sciences* 309, 315–318.
- Penaye, J., Toteu, S.F., Tchameni, R., Van Schmus, W.R., Tchakounté, J., Ganwa, A., Minyem, D., Nsifa, E.N., 2004. The 2.1 Ga West Central African belt in Cameroon: extension and evolution. *J. Afr. Earth Sc.* 39 (3–5), 159–164.
- Pimentel, M.M., Rodrigues, J.B., DellaGiustina, M.E.S., Junges, S., Matteini, M., Armstrong, R., 2011. The tectonic evolution of the Neoproterozoic Brasília Belt, central Brazil, based on SHRIMP and LA-ICPMS U-Pb sedimentary provenance data: a review. *J. S. Am. Earth Sci.* 31 (4), 345–357.
- Rubatto, D., Gebauer, D., 2000. Use of Cathodoluminescence for U-Pb Zircon Dating by Ion Microprobe: Some Examples from the Western Alps. In: Pagel, M., Barbin, V., Blanc, P., Ohnenstetter, D., (Eds.) *Cathodoluminescence in Geosciences*, pp. 373–400.
- Rudnick, R.L., Gao, S., 2003. Composition of the continental crust. In: Holland, H.D., Turekian, K.K. (Eds.), *The Crust Treatise on Geochemistry* 3. Elsevier-Pergamon, Oxford, pp. 1–64.
- Saha-Fouotsa, A.N., Vanderhaeghe, O., Barbey, P., Eglinger, A., Tchameni, R., Zeh, A., Tchunte, P.F., Nomo, E.N., 2019. The geologic record of the exhumed root of the Central African Orogenic Belt in the central Cameroon domain (Mbé-Sassa-Mbersi region). *J. Afr. Earth Sc.* 151, 286–314.
- Sepidbar, F., Mirnejad, H., Ma, C., 2018. Mineral chemistry and Ti in zircon thermometry: Insights into magmatic evolution of the Sangan igneous rocks, NE Iran. *Chimie der Erde-Geochemistry* 78 (2), 205–214.
- da Silva Filho, A.F., Guimarães, I.P., Ferreira, V.P., Armstrong, R., Sial, A.N., 2010. Ediacaran Águas Belas pluton, Northeastern Brazil: Evidence on age, emplacement and magma sources during Gondwana amalgamation. *Gondwana Res.* 17 (4), 676–687.
- Silva Filho, A.F., Guimaraes, I.P., Santos, L., Armstrong, R., Van Schmus, W.R., 2016. Geochronology, U-Pb geochronology, Sm-Nd and O isotopes of ca. 50 Ma long Ediacaran High-K Syn-Collisional Magmatism in the Pernambuco Alagoas Domain, Borborema Province, NE Brazil. *J. S. Am. Earth Sci.* <https://doi.org/10.1016/j.james.2015.12.013>.
- Silva Filho, A.F., Guimaraes, I.P., Van Schmus, W.R., Dantas, E., Armstrong, R., Concentino, L., Lima, D., 2013. Long-lived Neoproterozoic high-K magmatism in the Parnambuco-Alagoas domain, Borborema Province, North east Brazil. *Int. Geol. Rev.* 55, 1280–1299.
- Sláma, J., Kosler, J., Condon, D., Crowley, J., Gerdes, A., Hanchar, J., Horstwood, M., Morris, G., Nasdala, L., Norberg, N., 2008. Plesovice zircon-A new natural reference material for U-Pb and Hf isotopic microanalysis. *Chem. Geol.* 249 (1–2), 1–35.
- Smythe, D.J., Brenan, J.M., 2016. Magmatic oxygen fugacity estimated using zircon-melt partitioning of cerium. *Earth Planet. Sci. Lett.* 453, 260–266.
- Söderlund, U., Patchett, P.J., Vervoort, J.D., Isachsen, C.E., 2004. The 176 Lu decay constant determined by Lu-Hf and U-Pb isotope systematics of Precambrian mafic intrusions. *Earth Planet. Sci. Lett.* 219 (3–4), 311–324.
- Sun, S.S., McDonough, W.F., 1989. Chemical and isotopic systematics of oceanic basalts: implication for mantle composition and processes. In: Saunderson, A.D., Norry, M.J. (Eds.), *Magmatism in the Ocean Basins*. Geological Society, London, Special Publications 42, pp. 313–345.
- Sylvester, P.J., 1989. Post-collisional alkaline granites. *J. Geol.* 97 (3), 261–280.
- Tang, M., Wang, X.L., Shu, X.J., Wang, D., Yang, T., Gopon, 2014. Hafnium isotopic heterogeneity in zircons from granitic rocks: geochemical evaluation and modeling of "zircon effect" in crustal anatexis. *Earth Planet. Sci. Lett.* 389, 188–199.
- Taylor, S.R., McLennan, S.M., 1985. *The Continental Crust: Its Composition and Evolution*. Blackwell, Oxford, p. 312.
- Tchakounté, J., Eglinger, A., Toteu, S.F., Zeh, C., Nkoumbou, C., Mvondo Ondo, J., Penaye, J., De Wit, M., Barbey, P., 2017. The Adamawa-Yadé domain, a piece of

- Archaean crust in the Neoproterozoic Central African Orogenic belt (Bafia area, Cameroon). *Precambr. Res.* 299, 210–229.
- Tchakounté, J.N., Gentry, F.C., Kamwa, A.N., Victor, M., Ondo, J.M., Nkoumbou, C., 2021. Petrology and geochemistry of the Pan–African high–K calc–alkaline to shoshonitic-adakitic Bapé plutonic suites (Adamawa–Yade block, Cameroon): evidence of a hot oceanic crust subduction. *Int. J. Earth Sci.* 110 (6), 2067–2090.
- Tchameni, R., Pouclet, A., Penaye, J., Ganwa, A.A., Toteu, S.F., 2006. Petrography and geochemistry of the Ngaoundéré Pan-African granitoids in Central North Cameroon: Implications for sources and geological setting. *J. Afr. Earth Sc.* 44, 511–529.
- Tchouankoue, J.P., Li, X.-H., Ngo Belnoun, R.N., Mouafou, L., Pinto Ferreira, V., 2016. Timing and tectonic implications of the Pan-African Bangangte syenomonzonite, West Cameroon: Constraints from in-situ zircon U-Pb age and Hf-O isotopes. *J. Afr. Earth Sc.* 124, 94–103.
- Thiéblemont, D., Tegyey, M., 1994. Une discrimination géochimique des roches différenciées témoins de la diversité d'origine et de situation tectonique des magmas calco-alcalins. *Comptes Rendus Académie des Sciences, Paris* 319, 87–94.
- Toteu, S.F., Michard, A., Bertrand, J.M., Rocci, G., 1987. U/Pb dating of Precambrian rocks from northern Cameroon, orogenic evolution and chronology of the Pan-African belt of Central Africa. *Precambr. Res.* 37 (1), 71–87.
- Toteu, S.F., Penaye, J., Deloule, E., Van Schmus, W.R., Tchameni, R., 2006a. Diachronous evolution of volcano-sedimentary basins north of the Congo craton: Insights from U-Pb ion microprobe dating of zircons from the Poli Lom and Yaoundé Groups (Cameroon). *J. Afr. Earth Sc.* 44 (4–5), 428–442.
- Toteu, S.F., Penaye, J., Djomani, Y.P., 2004. Geodynamic evolution of the Pan-African belt in central Africa with special reference to Cameroon. *Can. J. Earth Sci.* 41 (1), 73–85.
- Toteu, S.F., Van Schmus, W.R., Penaye, J., Michard, A., 2001. New U-Pb and Sm-Nd data from north-central Cameroon and its bearing on the pre-Pan-African history of central Africa. *Precambr. Res.* 108 (1–2), 45–73.
- Toteu, S.F., Van Schmus, W.R., Penaye, J., Nyobe, J.B., 1994. U-Pb and Sm-Nd evidence Eburnean and Pan-African high grade metamorphism in cratonic rocks of Southern Cameroon. *Precambr. Res.* 67, 321–347.
- Toteu, S.F., Fouateu, R.Y., Penaye, J., Tchakounté, J., Mouangue, A.C.S., Van Schmus, W.R., Deloule, E., Stendal, H., 2006b. U-Pb dating of plutonic rocks involved in the nappe tectonic in southern Cameroon: consequence for the Pan-African orogenic evolution of the central African fold belt. *J. Afr. Earth Sc.* 44 (4–5), 479–493.
- Trail, D., Watson, E.B., Tailby, N.D., 2011. The oxidation state of Hadean magmas and implications for early Earth's atmosphere. *Nature* 480 (7375), 79–82.
- Trompette, R., 1997. Neoproterozoic (~600 Ma) aggregation of Western Gondwana: a tentative scenario. *Precambr. Res.* 82 (1–2), 101–112.
- Valeriano, C.M., Machado, N., Simonetti, A., Valladares, C.S., Seer, H.J., Simoes, L.S.A., 2004. U-Pb geochronology of the southern Brasília belt (SE-Brazil): sedimentary provenance, Neoproterozoic orogeny and assembly of West Gondwana. *Precambr. Res.* 130, 27–55.
- Valley, J.W., Chiarenzelli, J.R., McLellan, J.M., 1994. Oxygen isotope geochemistry of zircon. *Earth Planet. Sci. Lett.* 126 (4), 187–206.
- Valley, J.W., Lackey, J.S., Cavosie, A.J., Chechenko, C.C., Spicuzza, M.J., Basei, M.A.S., Bindeman, I.N., Ferreira, V.P., Sial, A.N., King, E.M., Peck, W.H., Sinha, A.K., Wei, C., 2005. 4.4 billion years of crustal maturation: oxygen isotope ratios of magmatic zircon. *Contrib. Miner. Petrol.* 150 (6), 561–580.
- van Schmus, W.R., Oliveira, E.P., da Silva Filho, A.F., Toteu, S.F., Penaye, J., Guimarães, I.P., 2008. Proterozoic links between the Borborema Province, NE Brazil, and the Central African Fold Belt. *Geol. Soc., London, Special Publ.* 294 (1), 69–99.
- Wang, W., Cawood, P.A., Pandit, M.K., Zheng, J.P., Zhao, J.H., 2019. No collision between Eastern and Western Gondwana at their northern extent. *Geology* 47, 308–312.
- Wang, W., Pandit, M.K., Zhao, J.H., Chen, W.T., Zheng, J.P., 2018. Slab break-off triggered lithosphere - asthenosphere interaction at a convergent margin: The Neoproterozoic bimodal magmatism in NW India. *Lithos* 296–299, 281–296.
- Watson, E.B., Harrison, T.M., 1983. Zircon saturation revisited: Temperature and composition effects in a variety of crustal magma types. *Earth Planet. Sci. Lett.* 64 (2), 295–304.
- Watson, E.B., Harrison, T.M., 2005. Zircon thermometer reveals minimum melting conditions on earliest Earth. *Science* 308 (5723), 841–844.
- Weecksteen, G., 1957. Carte géologique de reconnaissance à l'échelle du 1/500.000, feuille Douala-Est avec Notice explicative. Direction des Mines et de la Géologie, du Cameroun. 35, p.
- Wang, W., Cawood, P.A., Spencer, C.J., Pandit, M.K., Zhao, J.H., Xia, X.P., Zheng, J.P., Lu, G.M., 2022. Global-scale emergence of continental crust during the Mesoarchean–early Neoarchean. *Geology* 50 (2), 184–188.
- Wu, Y., Zheng, Y., 2004. Genesis of zircon and its constraints on interpretation of U-Pb age. *Chin. Sci. Bull.* 49 (15), 1554–1569.
- Yang, Q., Xia, X., Zhang, W., Zhang, Y., Xiong, B., Xu, Y., Wang, Q., Wei, G., 2018. An evaluation of precision and accuracy of SIMS oxygen isotope analysis. *Solid Earth Sci.* 3 (3), 81–86.
- Yomeun, B.S., Wang, W., Tchouankoue, J.P., Kamani, M.S.K., Ndofack, K.I.A., Huang, S.-F., Basua, E.A.A., Lu, G.-M., Xue, E.-K., 2022. Petrogenesis and tectonic implication of Neoproterozoic I-Type Granitoids and orthogneisses in the Gao-Mandja area. *Lithos* 106700.
- Yu, S., Sun, J., Evans, N.J., Danišík, M., Wu, L., Tian, Y., Shen, Z.e., 2020. Further Evaluation of Penglai Zircon Megacrysts as a Reference Material for (U-Th)/He Dating. *Geostand. Geanal. Res.* 44 (4), 763–783.
- Yu, Y., Sun, M., Long, X.P., Li, F., Zhao, G.C., Kröner, A., Broussolle, A., Yang, J.H., 2017. Whole-rock Nd-Hf isotopic study of I-type and peraluminous granitic rocks from the Chinese Altai: constraints on the nature of the lower crust and tectonic setting. *Gondwana Res.* 47, 131–141.
- Zeh, A., Gerdes, A., Barton, J., Klemd, R., 2010. U-Th-Pb and Lu-Hf systematics of zircon from TTG's, leucosomes, meta-anorthosites and quartzites of the Limpopo Belt (South Africa): Constraints for the formation, recycling and metamorphism of Palaeoarchean crust. *Precambr. Res.* 179 (1–4), 50–68.
- Zeh, A., Gerdes, A., Barton Jr., J.M., 2009. Archaean accretion and crustal evolution of the Kalahari Craton—the Zircon age and Hf isotope record of granitic rocks from Barberton/Swaziland to the Francistown Arc. *J. Petrol.* 50, 933–966.
- Zhang, C., Santosh, M., Luo, Q., Jiang, S., Liu, L., Liu, D., 2019. Impact of residual zircon on Nd-Hf isotope decoupling during sediment recycling in subduction zone. *Geosci. Front.* 10 (1), 241–251.